Chapter 8 – GROUND EXPERIMENTAL ACTIVITIES

8.1 GENERAL

Ground experiments performed during this research included Near Infrared (NIR) laser beam atmospheric propagation measurements, LTD/LRF pointing accuracy tests, systems harmonisation and performance evaluation trials of the PILASTER STU components. Furthermore, dedicated ground trials were performed with the LOAS system in order to assess its detection performance (in various weather conditions), and to verify the reliability of its obstacle classification algorithms. This chapter describes field trials and experiments carried out during the research. Particularly, tests objectives and procedures, instrumentation requirements and the data analysis methods are described, together with results of all ground experimental activities.

8.2 ATMOSPHERIC EXTINCTION MEASUREMENTS

In order to characterise atmospheric propagation at λ = 1064 nm and λ = 1550 nm, various tests were performed at the PISQ laser test range, using the PILASTER STU and additional instrumentation. Particularly, the following activities were performed:

- Determination of atmospheric extinction with different visibilities, temperatures, relative humidity values, wind intensities/directions, etc.; and
- Determination of atmospheric extinction with different types of rain (rainfall-rate, raindrops dimensions, etc.).

For this purposes, the ELOP-PLD and a modified version of the LOAS systems were used, in conjunction with suitable weather monitoring instrumentation. The primary aim of these test activities was to start data acquisition for compilation of a Laser Propagation Data Base (LPDB), necessary to validate/improve the propagation models used for simulation and analysis at the PILASTER range.

Propagation measurements at λ = 1064 nm were performed using the same basic equipment employed for the PILASTER STU, including detectors at the targets locations and NIR cameras for beam characterization (i.e., energy measurement systems). Furthermore, some additional instrumentation was used for performing extinction measurements at λ = 1550 nm, in conjunction with the modified LOAS system. During the measurements, a number of atmospheric parameters were monitored and recorded: meteorological visibility (V), temperature (T), relative humidity (RH), atmospheric pressure (P), wind direction and velocity (W_d and W_v), solar radiation (E_s), and cloud amount. The local atmospheric parameters were continuously measured/ recorded, during the test sessions, using the PILASTER meteorological instrumentation. These parameters were also monitored by the local Air Force Meteorological Office (some relevant vertical profiles were also determined with the aid of instrumented meteorological-balloons).

Meteorological data were collected at the PILASTER test range in different seasons and at different times of the day (4 times a day with 6 hours sampling intervals), in order to define a set of representative weather conditions for performing laser propagation measurements. The WMO scales used to classify cloud amount and horizontal visibility are defined in Table 8-1. The Cumulative Frequency Distribution Functions (CDF) relative to the data collected in the years 1998 – 2003 (divided in four groups of three months: Dec/Jan/Feb, Mar/Apr/May, Jun/Jul/Aug and Sept/Oct/Nov) are shown in the Figure 8-1 to Figure 8-3.

Table 8-1: WMO Scales Used to Classify Cloud Amount and Horizontal Visibility

WMO code	*Cloud amount*
0	No clouds
1	1/8
2	2/8
3	3/8
4	4/8
5	5/8
6	6/8
7	7/8
8	8/8
9	Upper air not visible

WMO code	*Horiz. visib.*
90	< 50 m
91	50-200 m
92	200-500 m
93	500-1000 m
94	1-2 km
95	2-4 km
96	4-10 km
97	10-20 km
98	20-50 km
99	>50 km

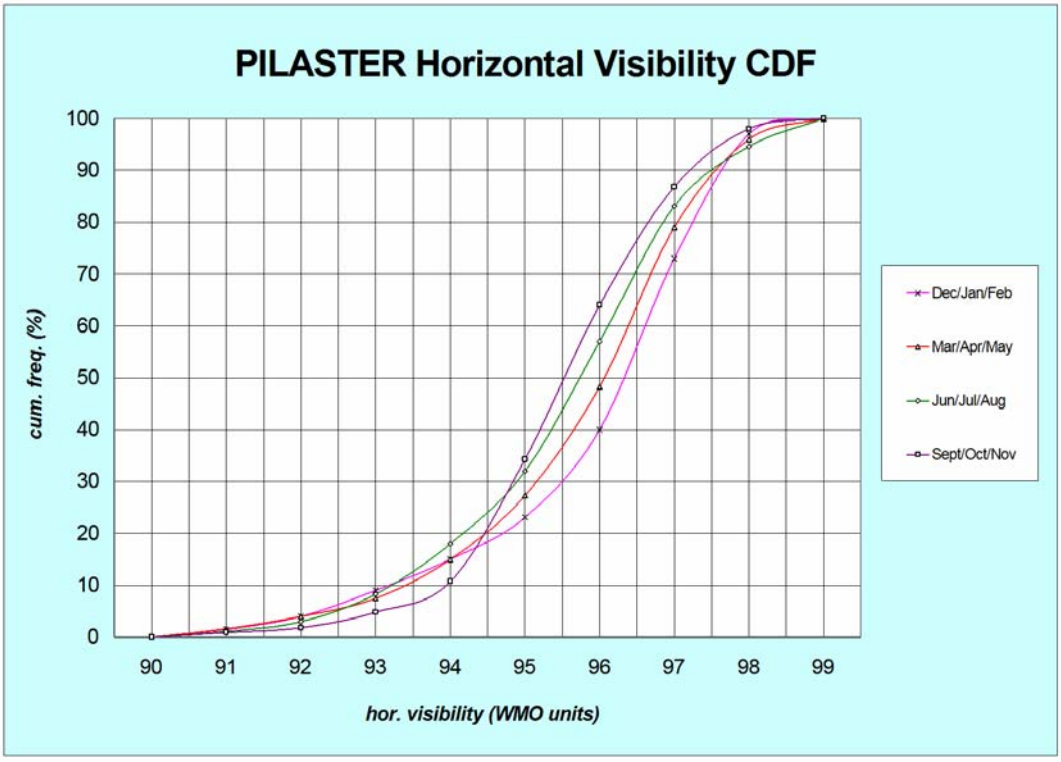

Figure 8-1: PILASTER Horizontal Visibility CDF (1998 – 2003).

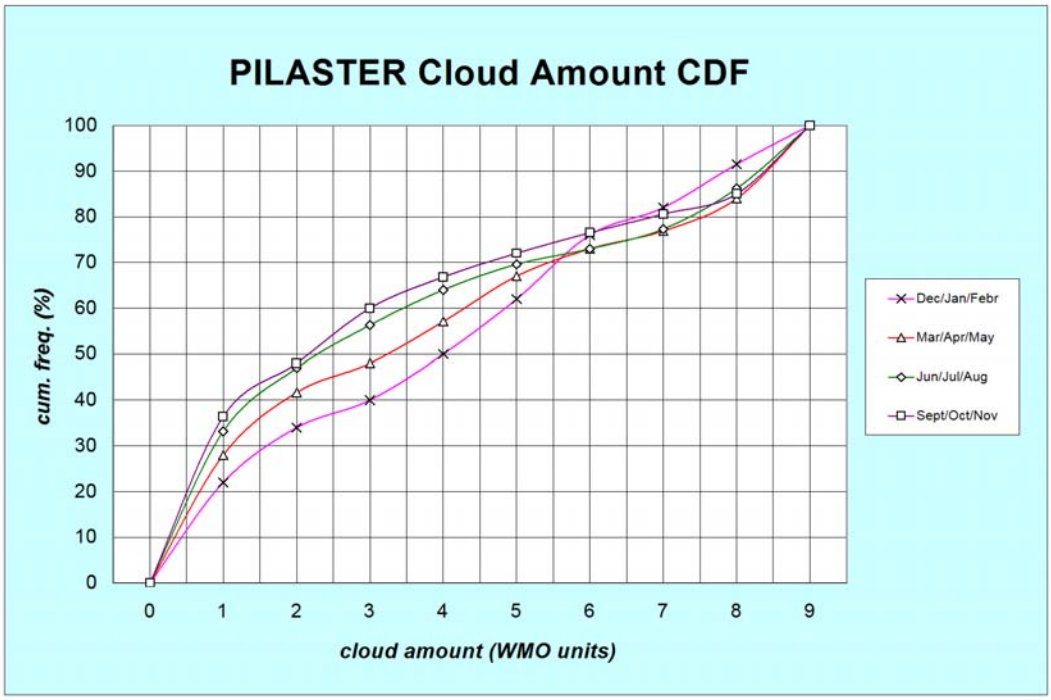

Figure 8-2: PILASTER Cloud Amount CDF (1998 – 2003).

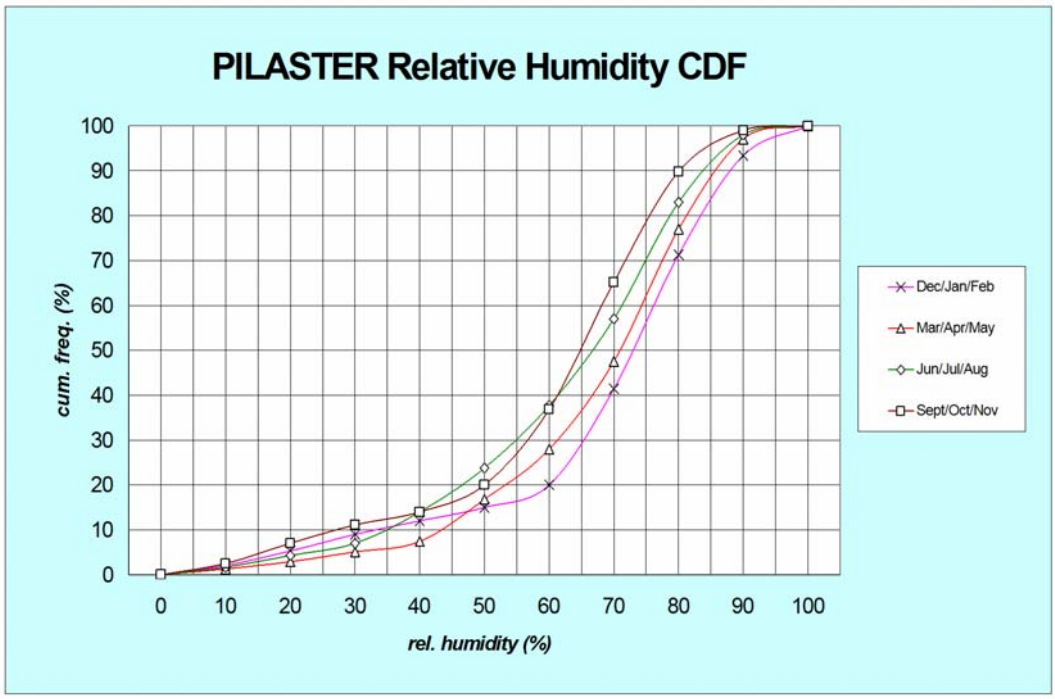

Figure 8-3: PILASTER Relative Humidity CDF (1998 – 2003).

The ELOP-PLD (λ = 1064 nm) and the LOAS (λ = 1550 nm) systems were used as the laser sources for propagation measurements. Particularly, in order to perform measurements at λ = 1550 nm the LOAS transmitter and receiver sub-systems were mounted on a tripod, as shown in Figure 8-4.

ELOP-PLD ***LOAS transmitter/receiver***

Figure 8-4: ELOP-PLD and Modified LOAS Systems.

The PILASTER test range areas used for laser beam propagation measurements and the locations of systems and targets used for tests at $\lambda = 1064$ nm and $\lambda = 1550$ nm are shown in Figure 8-5. More details about propagation tests geometries are presented later in this chapter.

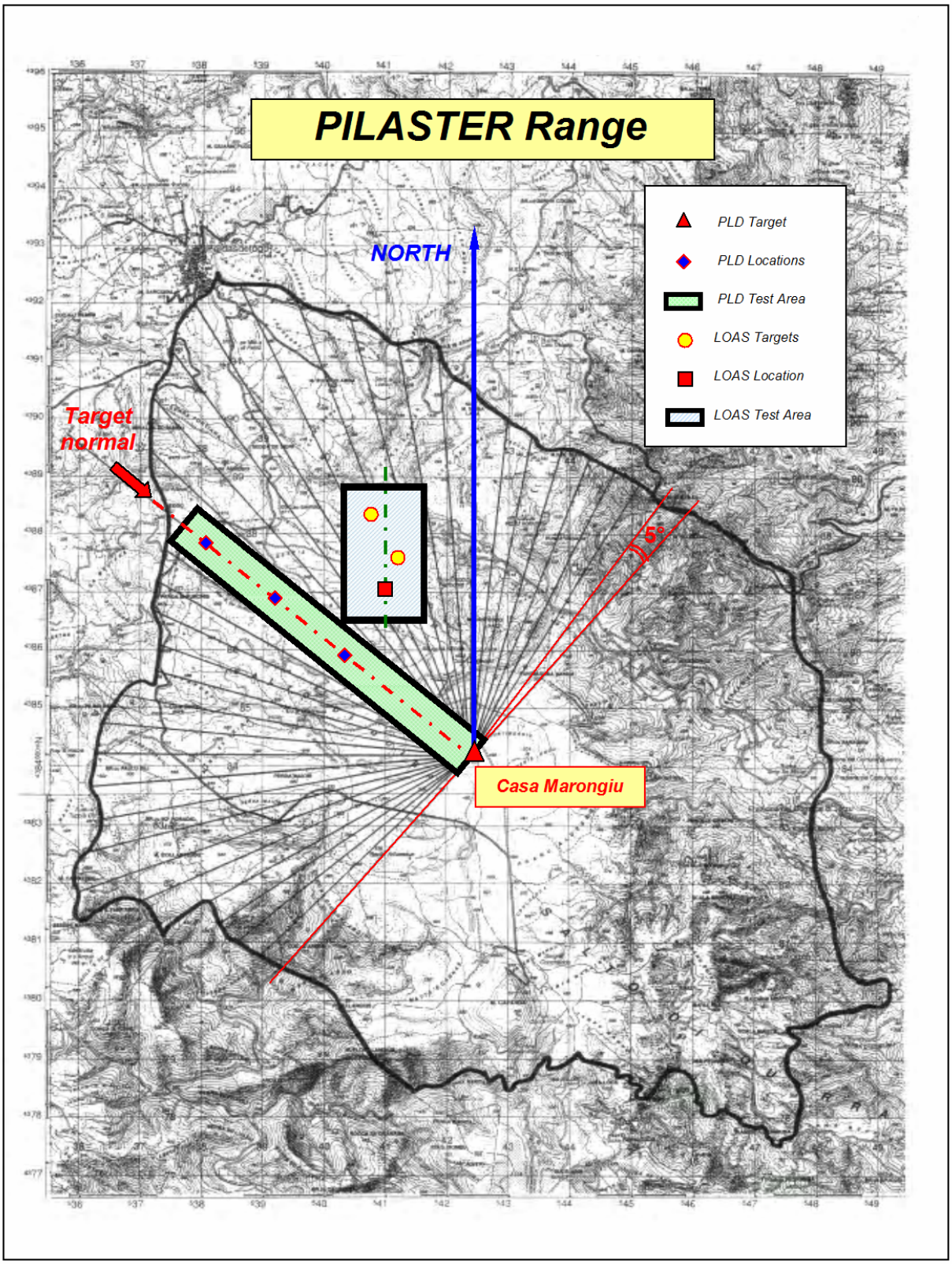

Figure 8-5: PILASTER Areas Used for Atmospheric Propagation Measurements.

The three techniques used for atmospheric propagation tests were the following:

- Extinction Measurement Technique N° 1 (EMT-1), employing PILASTER STU instrumentation (i.e., non-calibrated Phoenix NIR camera and PEP sensors), for measurements at $\lambda = 1064$ nm.
- Extinction Measurement Technique N° 2 (EMT-2), employing the PILASTER calibrated Phoenix NIR camera, for measurements at $\lambda = 1064$ nm.
- Extinction Measurement Technique N° 3 (EMT-3), specifically developed for measurements at $\lambda = 1550$ nm, using the modified LOAS system.

EMT-3 had to be adopted instead of EMT-1 and EMT-2 (PILASTER standard techniques), because the LOAS laser transmitter presented a PRF of 40 kHz, not compatible with the standard PILASTER STU sensors response. Therefore, the Phoenix NIR camera was filtered and calibrated only for measurements at $\lambda = 1064$ nm. Furthermore, a Control Technique (EMT-CT) was adopted for field calibration of the PILASTER EMT-1 and EMT-2. The EMT-1 and EMT-2 techniques were described in Chapter 5. The rationales of EMT-CT and EMT-3 are presented below.

8.2.1 EMT Control Technique (EMT-CT)

A control technique was adopted to verify the reliability and accuracy of the PILASTER EMT-1 and EMT-2. This control technique was based on a very simple concept (see Figure 8-6). Placing the PLD/LOAS systems and the PILASTER NIR camera (with appropriate optics) very close to the target surface (100 m and 80 m respectively) in conditions of very good visibility ($V > 20$ km) and low humidity ($RH < 65\%$ at $T < 25°$), it was reasonable to assume that the entire output laser energy reached the target surface (i.e., $\tau_{atm} \cong 100\%$), and that the NIR camera detected the whole laser spot energy.

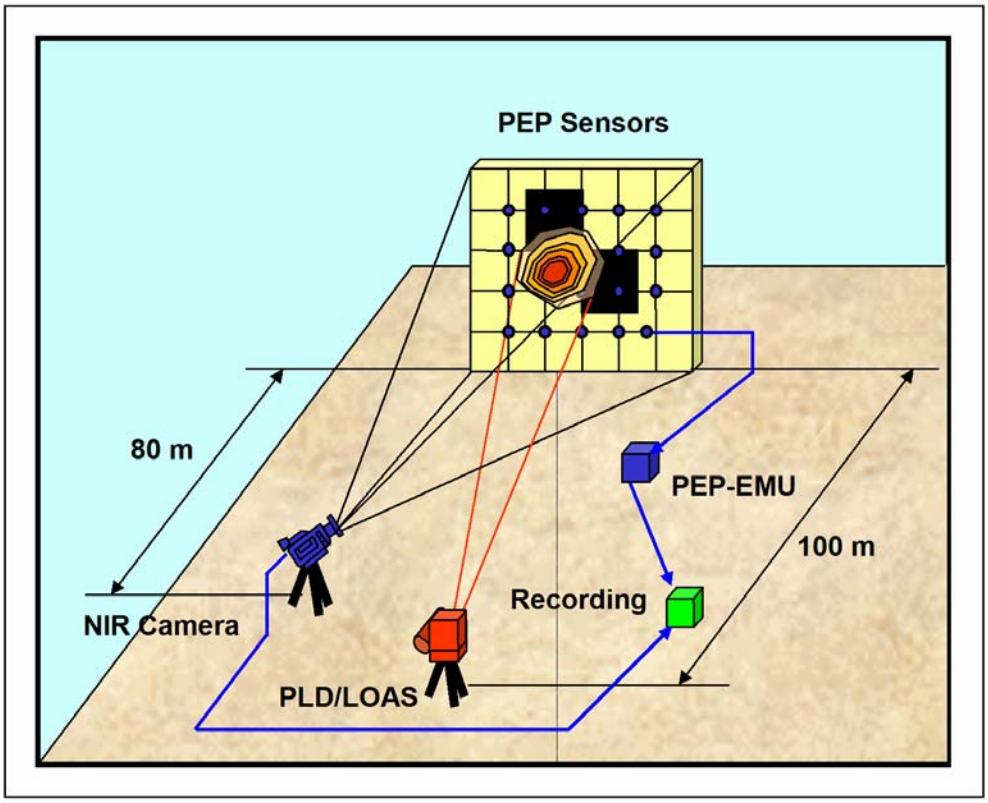

Figure 8-6: Experimental Arrangement for EMT-CT Tests.

Beam expansion and calibrated attenuation optics were used to conveniently modify the output laser beam for performing simultaneous NIR camera and PEP sensors measurements. Therefore, using the test instrumentation set up shown in Figure 8-6 and performing a large number of measurements, the errors of the PILASTER instrumentation in measuring atmospheric transmittance (EMT-1 and EMT-2) could be estimated by standard mathematical and statistical techniques.

8.2.2 Description of EMT-3

Since the LOAS laser transmitter presented a PRF of 40 kHz, not compatible with the standard PILASTER STU sensors response (*Phoenix* NIR camera full-frame), an additional technique was developed for performing atmospheric propagation measurements at $\lambda = 1550$ nm. This technique allowed indirect determination of atmospheric extinction measuring the LOAS transmitted laser power and the anodic voltage at the receiver. The rationale of this new technique is the following.

In general, the function describing the anodic voltage at the receiver can be expressed in the form:

$$V = R_L \cdot R_S \cdot P \tag{8.1}$$

where V is the anodic voltage, R_L is the anodic load (Ω), R_S is the detector responsivity (A/W), and P is the power reaching the receiver detector (W).

From the discussion about laser systems performance calculation (Chapter 3), assuming an extended target, the power at the detector can be expressed as follows:

$$P = K_{SYS} \cdot \rho \cdot \frac{1}{d_O^{\,2}} \cdot e^{-2\gamma d_O} \tag{8.2}$$

where ρ is the target reflectivity, d_O is the distance of the target from the transmitter/receiver, and γ is the extinction coefficient. K_{SYS} is a constant which accounts for all relevant transmitter/receiver systems parameters (e.g., transmitted laser power (P_O), efficiency of the transmitting and receiving optics (η_{TX}, η_{RX}), output beam diameter and divergence (D_L, α_T), transmitter/receiver LOS geometry).

Therefore, using two identical *Lambertian* targets placed at slant-ranges d_1 and d_2 respectively from the laser transmitter/receiver with a similar LOS geometry, and assuming that the extinction coefficient is constant in the slant-ranges considered, the following expressions can be written for the two anodic voltages measured at the receiver using Target N° 1 (V_1) and Target N° 2 (V_2):

$$V_1 = R_L \cdot R_S \cdot \left(K_{SYS} \cdot \rho \cdot \frac{1}{d_1^{\,2}} \cdot e^{-2\gamma d_1} \right) \tag{8.3}$$

$$V_2 = R_L \cdot R_S \cdot \left(K_{SYS} \cdot \rho \cdot \frac{1}{d_2^{\,2}} \cdot e^{-2\gamma d_2} \right) \tag{8.4}$$

It is reasonable to assume that, measuring the anodic voltages V_1 and V_2, all system parameters remain constant, except the transmitted laser power (P_O) which may vary significantly in the time intervals where the two measurement sessions are performed.

With these assumptions, we can write the following expressions:

$$V_1 = K \cdot P_{O1} \cdot \frac{e^{-2\gamma d_1}}{d_1^{\,2}} \tag{8.5}$$

$$V_2 = K \cdot P_{O2} \cdot \frac{e^{-2\gamma d_2}}{d_2^{\,2}} \tag{8.6}$$

where P_{O1} and P_{O2} are the transmitted laser powers, and the factor K contains all constant terms. Therefore:

$$\frac{V_1}{V_2} = \frac{P_{O1}}{P_{O2}} \cdot \frac{d_2^{\,2}}{d_1^{\,2}} \cdot e^{2\gamma(d_2 - d_1)} \tag{8.7}$$

and finally we obtain:

$$\gamma = \frac{1}{2\Delta d} \cdot \ln\left[\frac{\left(\frac{V_1}{P_{O1}}\right) \cdot d_1^{\,2}}{\left(\frac{V_2}{P_{O2}}\right) \cdot d_2^{\,2}}\right] \tag{8.8}$$

where the difference of the system to target slant-ranges (d_1 - d_2) has been replaced by the symbol Δd. It should be noted that all parameters contributing to the constant K do not affect the measurements (i.e., knowledge of these parameters is not required if their value remains constant during the measurements performed on Target N° 1 and N° 2). Obviously, the accuracy in the measurement of γ is affected by:

- The error in measuring the distances d_1 and d_2;
- The error in measuring the voltages V_1 and V_2; and
- The error in measuring the powers P_{O1} and P_{O2}.

Therefore, considering the errors relative to the measured parameters (σ_{d1}, σ_{d2}, σ_{V1}, σ_{V2}, σ_{PO1}, σ_{PO2}), we can write:

$$\begin{aligned}\sigma_\gamma^{\,2} = {} & \frac{1}{(2\Delta d)^2} \cdot \left(\frac{\sigma_{V_1}^{\,2}}{V_1^{\,2}} + \frac{\sigma_{V_2}^{\,2}}{V_2^{\,2}}\right) + \frac{1}{(2\Delta d)^2} \cdot \left(\frac{\sigma_{P_{O1}}^{\,2}}{P_{O1}^{\,2}} + \frac{\sigma_{P_{O2}}^{\,2}}{P_{O2}^{\,2}}\right) + \\ & + \frac{\gamma^2}{\Delta d^2} \cdot \left(d_2 + \frac{1}{\gamma}\right)^2 \cdot \frac{\sigma_{d_2}^{\,2}}{d_2^{\,2}} + \frac{\gamma^2}{\Delta d^2} \cdot \left(d_1 + \frac{1}{\gamma}\right)^2 \cdot \frac{\sigma_{d_1}^{\,2}}{d_1^{\,2}}\end{aligned} \tag{8.9}$$

Assuming that the error σ_d and the relative errors σ_V/V and σ_{PO}/P_O are the same for the measurements performed with Target N° 1 and Target N° 2, we have:

$$\sigma_\gamma^{\,2} = \frac{1}{2\Delta d^2} \cdot \left(\frac{\sigma_V^{\,2}}{V^2} + \frac{\sigma_{P_O}^{\,2}}{P_O^{\,2}}\right) + \frac{\gamma^2}{\Delta d^2} \cdot \left[\left(d_1 + \frac{1}{\gamma}\right)^2 \cdot \frac{\sigma_d^{\,2}}{d_1^{\,2}} + \left(d_2 + \frac{1}{\gamma}\right)^2 \cdot \frac{\sigma_d^{\,2}}{d_2^{\,2}}\right] \tag{8.10}$$

Rearranging the terms in eq. (8.10), we obtain:

$$\sigma_\gamma = \frac{1}{\Delta d} \cdot \sqrt{\left\{\frac{1}{2} \cdot \left(\frac{\sigma_V^{\,2}}{V^2} + \frac{\sigma_{P_O}^{\,2}}{P_O^{\,2}}\right) + \gamma^2 \cdot \left[\left(d_1 + \frac{1}{\gamma}\right)^2 \cdot \frac{\sigma_d^{\,2}}{d_1^{\,2}} + \left(d_2 + \frac{1}{\gamma}\right)^2 \cdot \frac{\sigma_d^{\,2}}{d_2^{\,2}}\right]\right\}} \tag{8.11}$$

Thus, it is evident that the error in the measurement of γ is strongly affected by the distance between the two targets. For instance, in the case of the LOAS transmitter/receiver parameters, σ_V/V = 5% and σ_{PO}/P_O = 2%. Assuming σ_d = 1 m, d_1 = 800 m, Δd = 100 m, d_2 = 800 m, $\gamma = 7 \times 10^{-4}$ m^{-1}, from eq. (8.11)

we obtain a relative measurement error σ_γ/γ of about 54%. Obviously, doubling the distance between the two targets (e.g., assuming Δd = 200 m and d_2 = 1000 m), the estimated relative error would be 27% (half of the previous case). The experimental arrangement used for the extinction measurements at λ = 1550 nm is shown in Figure 8-7.

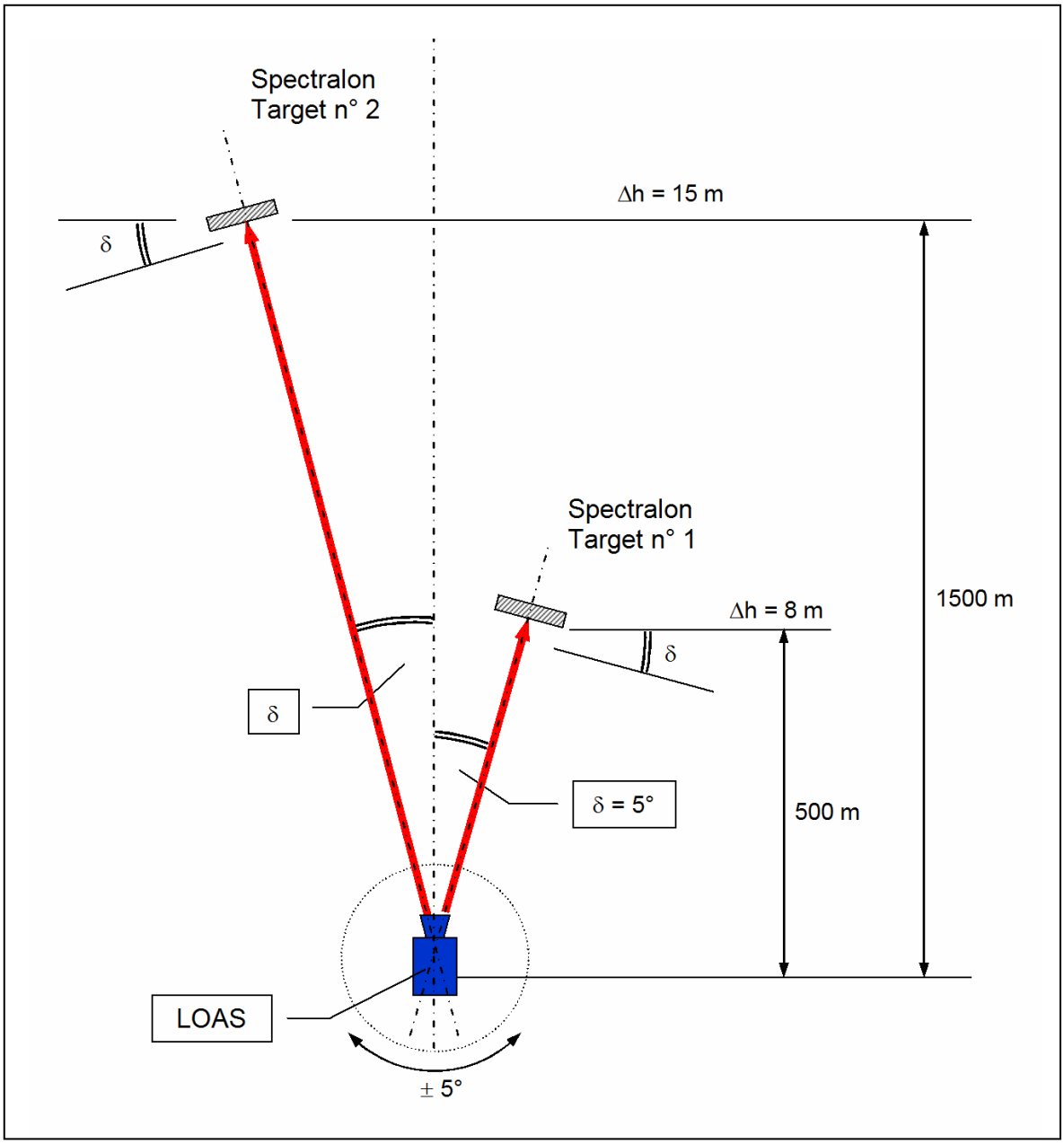

Figure 8-7: Experimental Arrangement for Propagation Tests at λ = 1550 nm.

Since the LOAS and the targets co-ordinates were determined by means of Differential GPS (DGPS) static surveys, we had $\sigma_d \leq 0.01$. Therefore:

$$\frac{1}{2}\cdot\left(\frac{\sigma_V^{\,2}}{V^2}+\frac{\sigma_{P_O}^{\,2}}{P_O^{\,2}}\right) >>> \gamma^2\cdot\left[\left(d_1+\frac{1}{\gamma}\right)^2\cdot\frac{\sigma_d^{\,2}}{d_1^{\,2}}+\left(d_2+\frac{1}{\gamma}\right)^2\cdot\frac{\sigma_d^{\,2}}{d_2^{\,2}}\right] \tag{8.12}$$

and:

$$\sigma_\gamma \cong \frac{1}{\Delta d} \cdot \sqrt{\frac{1}{2} \cdot \left(\frac{\sigma_V{}^2}{V^2} + \frac{\sigma_{P_O}{}^2}{P_O{}^2} \right)} \tag{8.13}$$

As in our case Δd = 1000 m, the estimated measurement error was:

$$\sigma_\gamma \cong \frac{1}{\Delta d} \cdot \sqrt{\frac{1}{2} \cdot \left(\frac{\sigma_V{}^2}{V^2} + \frac{\sigma_{P_O}{}^2}{P_O{}^2} \right)} = 3.81 \cdot 10^{-5}\ \mathrm{m}^{-1} \tag{8.14}$$

Therefore, since in general $\gamma > 10^{-4}$ m^{-1}, we calculated a maximum relative error σ_γ/γ of about 4%.

8.2.3 Verification and Optimisation of EMT-1 and EMT-2

During the initial phases of the experimental activity, it was understood that *Phoenix* NIR camera frame rate optimisation was crucial to data acquisition for both PILASTER techniques (EMT-1 and EMT-2), as well as to definition of the DAS (Digital Acquisition and Data Recording System) memory requirements for NIR camera data recording. Furthermore, significant differences were observed between the transmittance measurements obtained using EMT-1/EMT-2 and the transmittance values predicted by mathematical models. This aspect also had to be investigated to allow practical implementation of EMT-1 and EMT-2 at the PILASTER. Therefore, some ground experimental activities were performed in order to:

- Optimise the NIR camera frame rates for data acquisition at the PILASTER with state-of-the-art systems having pulse durations P_D < 20 ns and pulse repetition frequencies (PRF) between 10 Hz and 40 kHz (e.g., 10 or 20 Hz for ELOP-PLD, and 40 kHz for LOAS);
- Determine the computer memory requirements for NIR camera data recording at 10 Hz/20 Hz (ELOP-PLD) and 40 kHz (LOAS); and
- Evaluate/improve both EMT-1 and EMT-2 for measurements at λ = 1064 nm.

Phoenix NIR camera frame rate optimisation was carried out with preliminary calculations and two separated experimental sessions performed with the ELOP-PLD and the LOAS systems. During the same sessions, it was also verified the compatibility of the NIR camera frame rates with the commercial PC memories installed in the Phoenix DAS system. Evaluation of the PILASTER EMT-1/EMT-2 reliability was obtained by performing various test sessions with the PLD system, using EMT-CT. With this control techniques, it was also possible to determine useful correction for the EMT-1 and EMT-2 measurements at λ = 1064 nm.

8.2.3.1 NIR Camera Frame Rate Optimisation

After the initial ground tests with the NIR camera, it was decided that the NIR camera acquisition windows were not synchronised with the laser pulses incident on the target surface. In fact, although the NIR camera could be triggered by the laser pulses incident on the target using the PILASTER instrumentation, good synchronisation became extremely difficult even at low PRF and almost impossible as the PRF increased (also due to the existence of dark zones in the NIR camera acquisition windows). Therefore a preliminary study was required in order to determine optimal frame rates for the NIR camera acquisition as a function of the known laser pulses parameters. After that, some experimental sessions were performed to verify the validity of the models developed.

8.2.3.2 Frame Rate Optimisation Analysis

Let us consider the train of pulses shown in Figure 8-8. The parameters describing the train of pulses are the pulse duration (τ), the pulse period (T_P) and the PRF (f) given by:

$$f = \frac{1}{T_P} \tag{8.15}$$

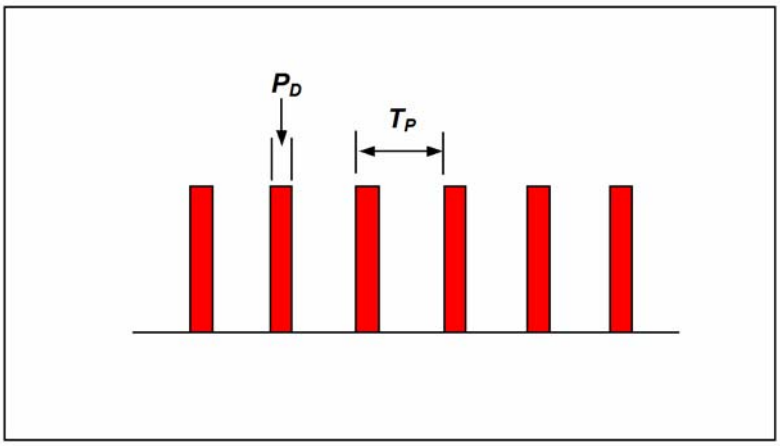

Figure 8-8: Train of Pulses.

The NIR camera image acquisition process is defined by the frame period (T_F) and the corresponding frame frequency (f_F) given by:

$$f_F = \frac{1}{T_F} \tag{8.16}$$

Each frame consists of a 320×256 pixels matrix. In general, the NIR camera real acquisition time (T_A) is inferior to the corresponding framing window defined by T_F. The difference between T_F and T_A is the so called camera 'dark-time' (T_{dark}). For the Phoenix camera T_{dark} is 2% of the frame period (T_F). Therefore:

$$T_{dark} = T_{dark\%} \cdot T_f = 0.02 \cdot T_f \tag{8.17}$$

$$T_A = T_F - 0.02 \cdot T_f \tag{8.18}$$

A schematic representation of the NIR camera acquisition windows and dark zones is shown in Figure 8-9.

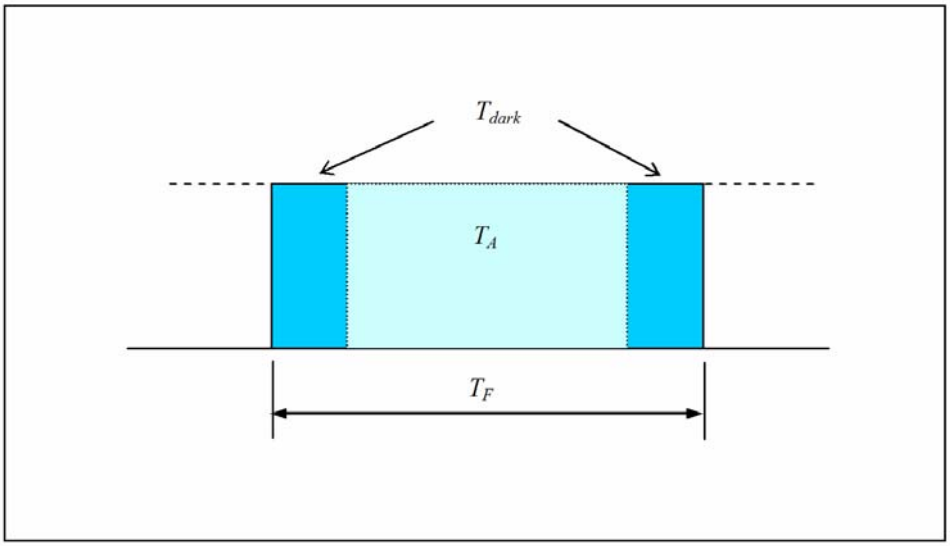

Figure 8-9: NIR Camera Acquisition Windows and Dark Zones.

Since the NIR camera frames are not synchronised with the laser pulses, considering the NIR camera acquisition windows sequence as our time base (T_b), the instant of arrival of the first laser pulse (reflected from the target) at the NIR camera (T_o) can be treated as a random variable (see Figure 8-10).

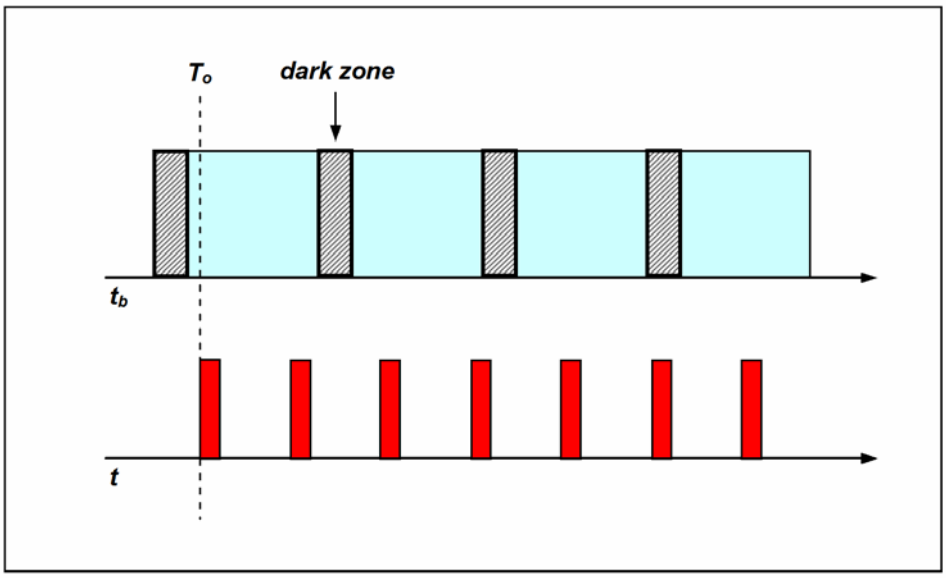

Figure 8-10: NIR Camera Acquisition Windows Sequence and Laser Pulses.

Therefore, our optimisation problem consists in determining the frame period (T_F) satisfying the following conditions:

Cond. 1 → Only one pulse has to be acquired in a single frame.

Cond. 2 → The probability of a laser pulse being entirely or partially in the dark zones of the NIR camera acquisition windows sequence has to be minimised.

To satisfy the first condition, we set:

$$T_F \leq T_P \tag{8.19}$$

Since we consider as 'error' the event of a laser pulse being totally or partially in the 'dark zones', we have to take into account the duration of the laser pulses (τ) in our analysis. To simplify calculations, we model the laser pulses as pure *Dirac*-pulses (i.e., pulses of zero duration), simply by adding τ to the dark periods (T_{dark}) at the beginning and at the end of the acquisition windows (Figure 8-11). Therefore, we define the 'effective dark time' (T_{dark_eff}) as follows:

$$T_{dark_eff} = T_{dark\%} T_F + \tau \tag{8.20}$$

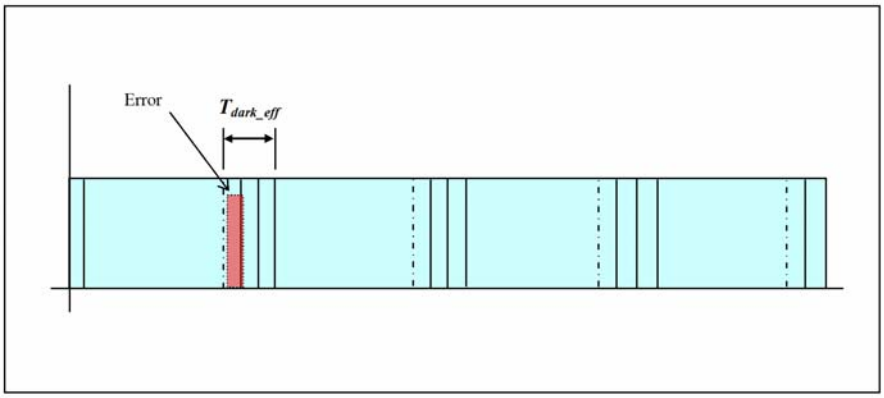

Figure 8-11: Effective Dark Time.

The resulting model used for analysis is shown in Figure 8-12.

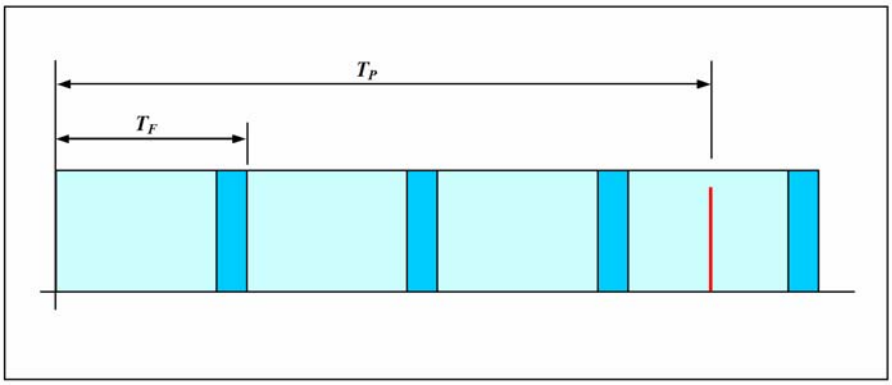

Figure 8-12: Model Used for Analysis.

Having defined our reference windows sequence, we have to choose the probability distribution modelling the arrival of a laser pulse into windows sequence. Since $T_F \leq T_P$, in a single pulse period there may be various acquisition windows. Therefore, knowing that in the time interval [0; T_P] only one pulse has to be present, we model the time of arrival of the laser pulse as a uniform random variable (Figure 8-13).

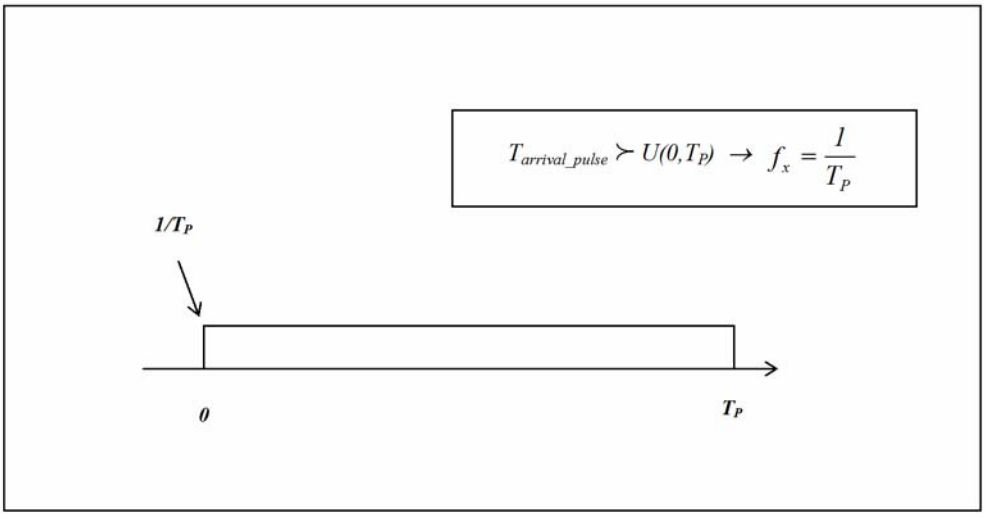

Figure 8-13: Probability Distribution for Pulse Time of Arrival.

The error probability with varying T_F is given by:

$$P_{err} = \int_{dark\ zones} \frac{1}{T_P} dx \tag{8.21}$$

We have the two cases described below.

Case-1: In the interval [0; T_P] there is an integer number of dark zones. Thus, the error probability becomes:

$$P_{err} = N_d \frac{T_{dark_eff}}{T_P} \tag{8.22}$$

Where N_d is the number of dark zones in the interval [0; T_P].

Case-2: In the interval [0; T_P] there is a decimal number of dark zones (Figure 8-14).

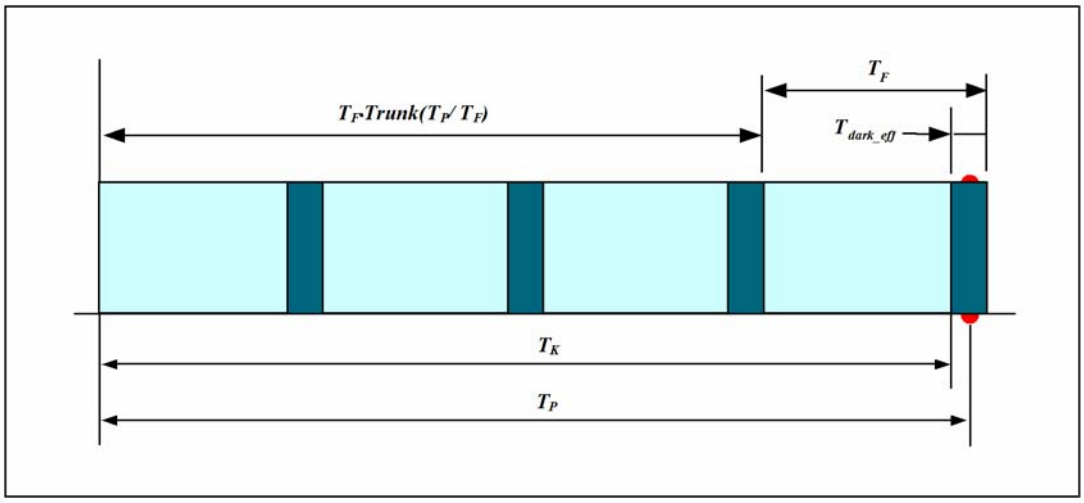

Figure 8-14: Decimal Number of Dark Zones in the Interval [0; T_P].

For our analysis, *Case-2* represents the general case (i.e., includes *Case-1*). As we notice in Figure 8-14, we have an integer number of dark zones plus a fraction of dark zone partially included in the interval [0; T_P]. Therefore, if we let:

$$T_K = T_F\left[1 + Trunk\left(T_P / T_F\right)\right] - T_{dark_eff} \tag{8.23}$$

the error probability in the general case is given by:

$$P_{err} = Trunk\left(\frac{T_P}{T_F}\right)\frac{T_{dark_eff}}{T_P} + \left(\frac{1}{T_P}\int_{T_K}^{T_P} dx\right)\cdot b \tag{8.24}$$

where b is a Boolean variable of the form:

$$\begin{cases} 1 \\ 0 \end{cases} \text{ if } T_P - T_F\left[1 + Trunk\left(\frac{T_P}{T_F}\right)\right] + T_{dark_eff} \begin{cases} > 0 \\ < 0 \end{cases} \tag{8.25}$$

Therefore, we obtain:

$$P_{err} = \left[Trunk\left(T_P / T_F\right) + \frac{1}{T_P}\left\{T_P + T_{dark_eff} - T_F\left[1 + Trunk\left(T_P / T_F\right)\right]\right\}\cdot b\right]\frac{T_{dark_eff}}{T_P} \tag{8.26}$$

where the number of dark zones in the interval [0; T_P] is:

$$N_D = Trunk\left(T_P / T_F\right) + \frac{1}{T_P}\left\{T_P + T_{dark_eff} - T_F\left[1 + Trunk\left(T_P / T_F\right)\right]\right\}\cdot b \tag{8.27}$$

Substituting eq. (8.20) into eq. (8.26), taking into account the eq. (8.25), we obtain the expressions of P_{err} listed in Table 8-2, where the function P_{err} has been defined with $N = 1,2,3\ldots$

Table 8-2: Error Probability (P_{err}) Equations in the Definition Intervals

T_F	P_{err}
$\frac{T_P + \tau_{pulse}}{2(1 - T_{dark\%}/2)} < T_F < T_P$	$\frac{T_{Buio\%}}{T_P} T_F + \frac{\tau_{pulse}}{T_P}$
$\frac{T_P}{2} < T_F < \frac{T_P + \tau_{pulse}}{2(1 - T_{dark\%}/2)}$	$\left(\frac{T_{dark\%}}{T_P} T_F + \frac{\tau_{pulse}}{T_P}\right) \times \left[1 + \frac{T_P + (T_{dark\%} - 2)T_P + \tau_{pulsee}}{\tau_{pulse} + T_{dark\%} T_F}\right]$
. . .	. . .
$\frac{T_P + \tau_{pulse}}{(N+1)(1 - T_{dark\%}/(N+1))} < T_F < \frac{T_P}{N}$	$N\left(\frac{T_{dark\%}}{T_P} T_F + \frac{\tau_{pulse}}{T_P}\right)$
$\frac{T_P}{(N+1)} < T_F < \frac{T_P + \tau_{pulse}}{(N+1)[1 - T_{dark\%}/(N+1)]}$	$N\left(\frac{T_{dark\%}}{T_P} T_F + \frac{\tau_{pulse}}{T_P}\right) \times \left[N + \frac{T_P + (T_{dark\%} - (N+1))T_P + \tau_{pulse}}{\tau_{pulse} + T_{dark\%} T_F}\right]$
. . .	. . .

The function P_{err}, calculated for f = 10 Hz and τ_{pulse} = 19 nsec (ELOP-PLD system) is shown in Figure 8-15.

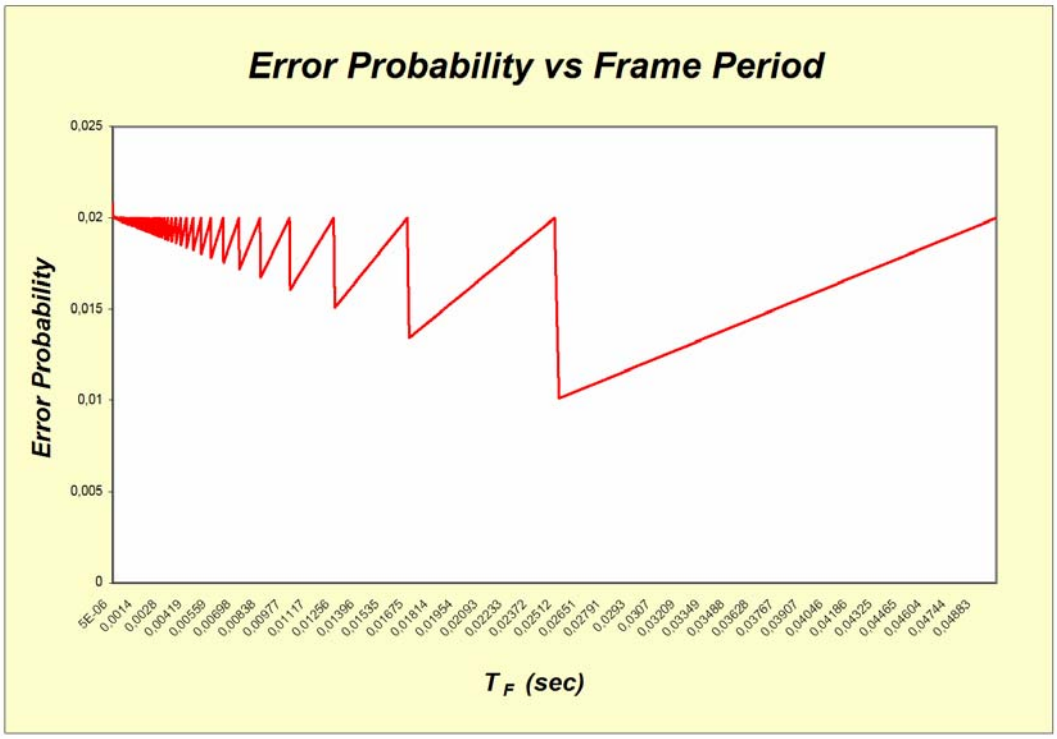

Figure 8-15: NIR Camera Error Probability Function for *f* = 10 Hz.

In general, the relative minimums of the error probability function are found for:

$$T_F = \frac{T_P + \tau_{pulse}}{(N+1)\left(1 - \frac{T_{dark\%}}{N+1}\right)} \tag{8.28}$$

giving the following values of P_{err}:

$$P_{Err} = N \frac{T_P + \tau_{pulse}}{(N+1)\left(1 - \frac{T_{dark\%}}{N+1}\right)} \frac{T_{dark\%}}{T_P} + \frac{N\tau_{pulse}}{T_P} \tag{8.29}$$

The absolute minimum (optimal) value of P_{err} is found for:

$$T_{F_opt} = \frac{T_P + \tau_{pulse}}{2\left(1 - \frac{T_{dark\%}}{2}\right)} \tag{8.30}$$

giving:

$$P_{Err_opt} = \frac{T_P + \tau_{pulse}}{2\left(1 - \frac{T_{dark\%}}{2}\right)} \frac{T_{dark\%}}{T_P} + \frac{\tau_{pulse}}{T_P} \tag{8.31}$$

In most cases of practical interest, and particularly for both the ELOP-PLD and LOAS systems (i.e., τ_{pulse} < 20 ns and 10 Hz < f < 40 kHz), we have that $T_P >>> \tau_{pulse}$. Therefore, the equations (8.30) and (8.31) become:

$$T_{F_opt} = \frac{T_P + \tau_{pulse}}{2\left(1 - \frac{T_{dark\%}}{2}\right)} \cong \frac{T_P}{2\left(1 - \frac{T_{dark\%}}{2}\right)} \cong \frac{T_P}{2} \tag{8.32}$$

$$P_{Err_opt} = \frac{T_P + \tau_{pulse}}{2\left(1 - \frac{T_{dark\%}}{2}\right)} \cdot \frac{T_{dark\%}}{T_P} + \frac{\tau_{pulse}}{T_P} \cong \frac{T_P}{2\left(1 - \frac{T_{dark\%}}{2}\right)} \cdot \frac{T_{dark\%}}{T_P} \cong \frac{T_P}{2} \cdot \frac{T_{dark\%}}{T_P} = \frac{T_{dark\%}}{2} \tag{8.33}$$

Let us now try to interpret the behaviour of the function P_{err} taking into account the physics involved. We know that the error probability is a function of the total dark time (i.e., the sum of all dark intervals in the acquisition windows) in the pulse period. Therefore, we deduce that increasing the number of acquisition windows in the same pulse period would produce more dark intervals (i.e., the overall dark time would increase), with the consequence that P_{err} would also increase. This is confirmed by the general trend of the P_{err} function which decreases as T_F increases. However, we have to explain why the function P_{err} experiences sudden increases at the points where T_P is a multiple integer of T_F.

Using eq. (8.20), considering that $T_{dark\%}$ = 2% for the NIR camera, and that τ_{pulse} < 20 nsec, we can write:

$$T_{dark_eff} = T_{dark\%} T_F + \tau_{pulse} \cong T_{dark\%} T_F \tag{8.34}$$

Therefore, since T_{dark_eff} is a fraction ($T_{dark\%}$) of the acquisition window, in the particular cases where T_P is a multiple integer of the acquisition window, the total dark time does not vary. In fact, if we consider n windows in the interval [0; T_P], we will have n dark intervals, with a total dark time given by:

$$T_{dark_tot} = n T_{dark\%} T_{F1} \tag{8.35}$$

Obviously, for n = 1 $T_{dark_tot} = T_{dark\%} T_F$, but $T_F = N T_{F1}$ and, therefore, as the total dark time does not vary, the error probability is the same. This is why all points of maximum have the same value for T_F far from zero. As T_F gets closer to zero, τ_{pulse} becomes significant, but this is a characteristic not useful for our analysis. Therefore, the graph in Figure 8-15 tells us that, with a given T_P, the value of T_{dark_tot} (and T_{dark_eff}) decreases as T_F decreases, up to the point where the dark zone of the last frame enters the interval [0; T_P]. When this happens, T_{dark_tot} (and T_{dark_eff}) goes back to the previous value, but then immediately starts to decrease again. Consequently, the minimum of P_{err} does not occur exactly at $T_F = T_P/2$, but for a value of T_F a bit greater than $T_P/2$, which would guarantee the first pulse to be just outside the dark zone of the second frame (Figure 8-16).

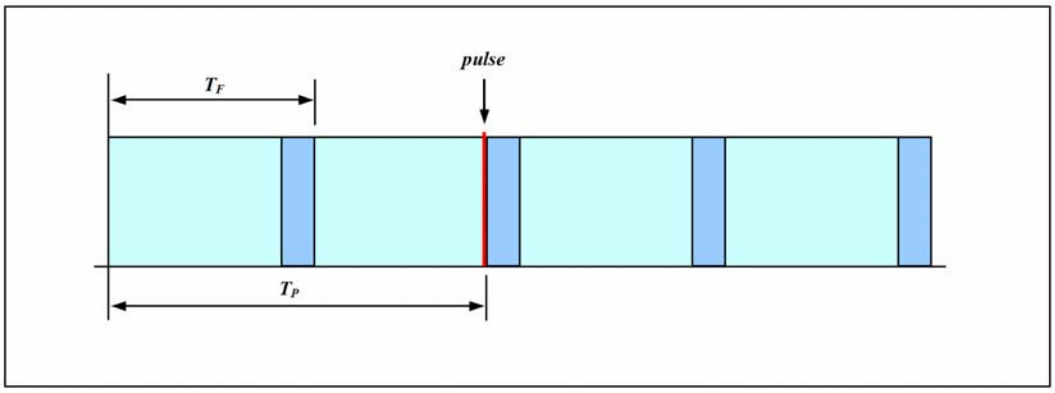

Figure 8-16: Condition of Minimum Error Probability.

We can now select the optimal frame rate (F_{F_opt}) for f = 10 Hz (i.e., ELOP-PLD Band N° 1). As explained before, if the T_F could be set at exactly $T_P/2$ minus a small quantity (e.g., $T_F = (T_P/2)-10^{-4}$), our optimisation problem was solved. However, as T_F (and F_F) is affected by instability (i.e., a variance σ_{TF} in the order of 10^{-4} sec about the nominal T_F), in order to avoid a possible increase of the P_{err}, it is convenient to chose our optimal T_F at about $2\sigma_{TF}$ from the $T_P/2$ point. This is shown in Figure 8-17, where it is evidenced that the T_F instability may cause the error to be maximised for a value of T_F not sufficiently greater that $T_P/2$ (Case 1). The improvement (reduction of P_{err}) is evident with $T_F = 2\sigma_{TF} + T_P/2$ (Case 2). Therefore, in terms of frame rate optimisation, we can write:

$$F_{F_opt} = 2\left(f - \sigma_{F_F}\right) \tag{8.36}$$

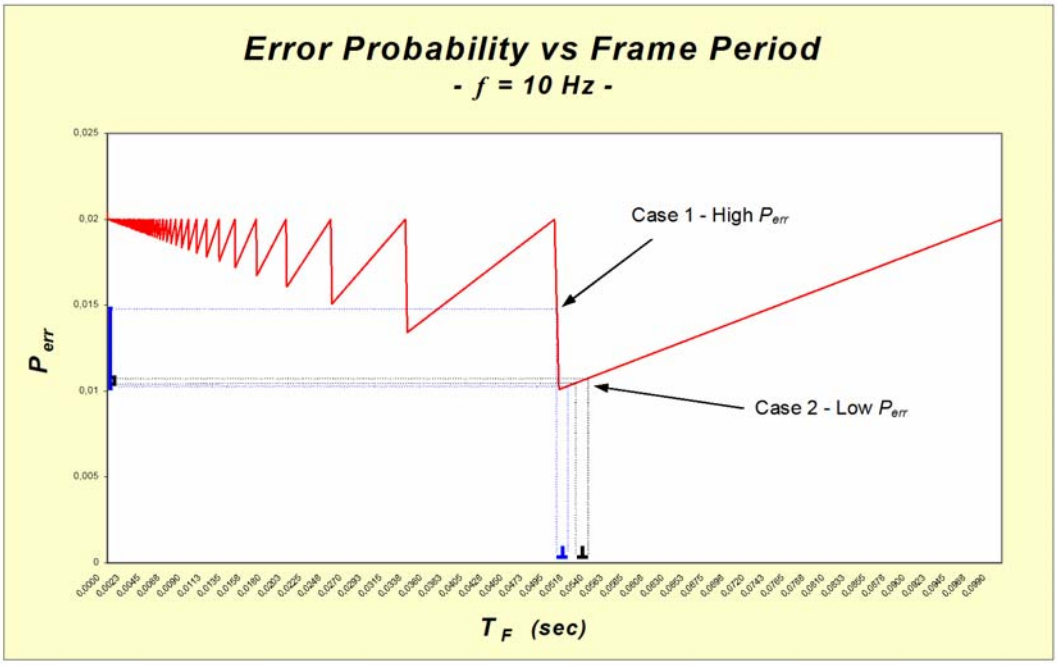

Figure 8-17: Effects of T_F Uncertainty on P_{err} for f = 10 Hz.

As the P_{err} function and σ_{TF} do not vary significantly up to f = 345 Hz for full frame NIR camera acquisition, the same optimisation criteria applies for f = 20 Hz (i.e., ELOP-PLD Band N° 2).

Let us now consider the case of f = 40 kHz (i.e., LOAS system). In this case, the function P_{err} previously defined, has the behaviour shown in Figure 8-18. Again, the first part of the function, where T_F is still close to the pulse duration, is not interesting for our analysis. We notice that, also in this case, the minimum P_{err} is found for a T_F of about $T_P/2$. However, as in this case the variance of T_F (σ_{T_F}) is in the order of about 10^{-5} sec, it is convenient to choose a T_F intermediate between $T_P/2$ and T_P (see Figure 8-18). Therefore:

$$T_{F_opt}' = \frac{3}{4} T_P \tag{8.37}$$

$$F_{F_opt}' = \frac{4}{3} f \tag{8.38}$$

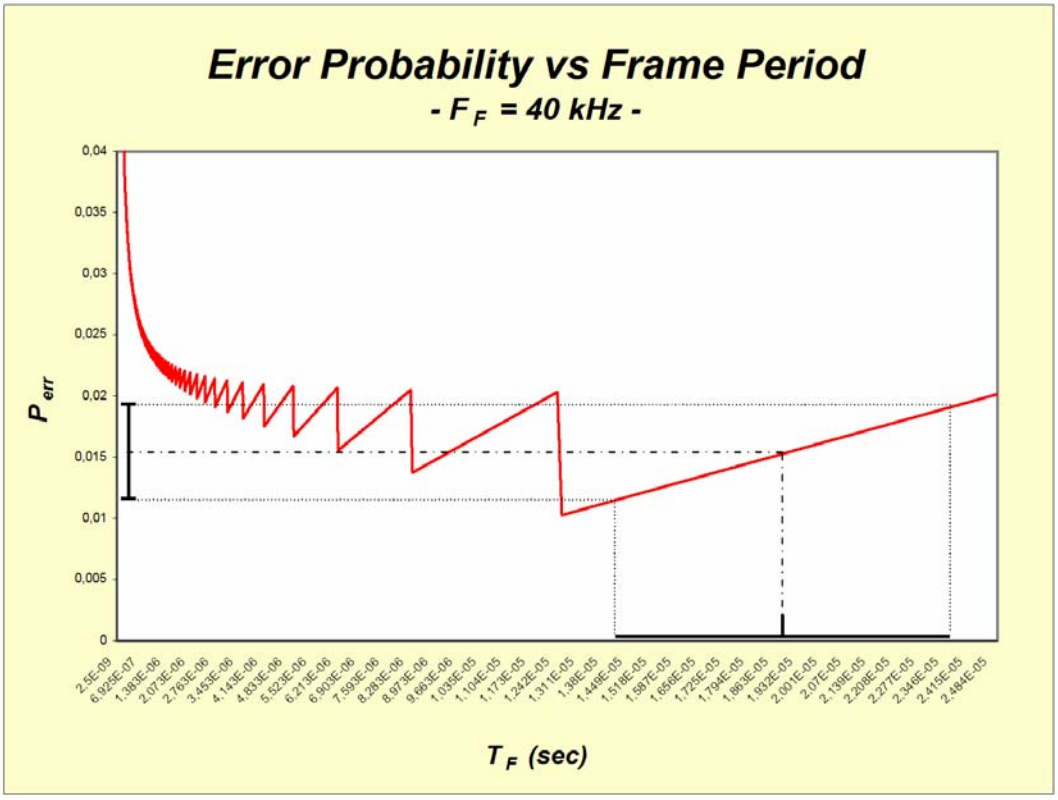

Figure 8-18: Effects of T_F Uncertainty on P_{err} for f = 40 kHz.

The results of the frame rate optimisation analysis, referred to the two boundary conditions f = 10 Hz (i.e., ELOP-PLD) and f = 40 kHz (i.e., LOAS) are summarised in Figure 8-19.

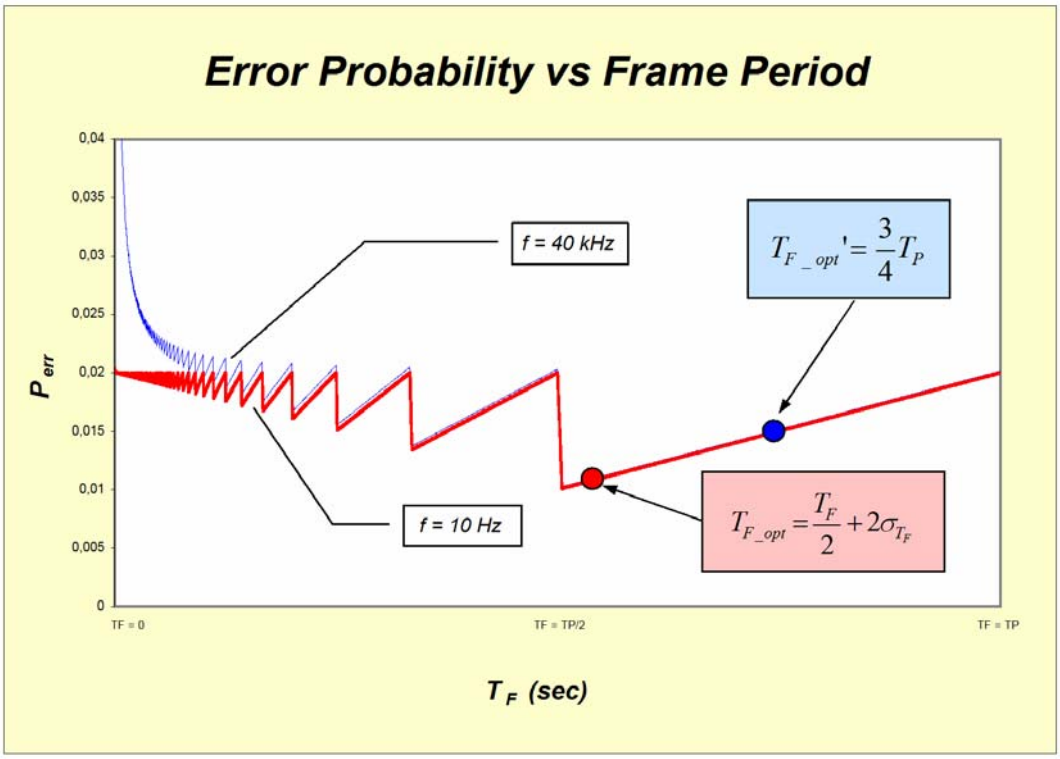

Figure 8-19: Results of NIR Camera Frame Rate Optimisation Analysis.

8.2.3.3 Frame Rate Optimisation Tests

In order to verify the results of the optimisation analysis, and to find good compromises for the NIR camera F_F applicable to the real cases, two dedicated ground test sessions were performed using the PLD and LOAS systems, with laser pulse repetition frequencies (f) of 10 Hz, 20 Hz (ELOP-PLD) and 40 kHz (LOAS). From eq. (8.36), the optimal F_F for f = 10 Hz was about 19.9997 Hz, and for f = 20 Hz was about 39.9997 Hz. However, as the NIR camera F_F settings were only possible with steps of 0.5 Hz, to avoid sudden increases of P_{err} (see discussion in Section 8.1.1.1), F_F was set to 19.5 Hz in the first case and to 39.5 Hz in the second case. From eq. (8.38), the optimal F_F for f = 40 kHz (LOAS system) was about 53 kHz. Unfortunately, the upper F_F limit of the Phoenix NIR camera with DAS was 38 kHz in smallest window (2 × 128 pixels) and 345 in full frame (320 × 256 pixels). Therefore, in this case it was not possible to use the NIR camera for full frame data recording (and therefore for EMT-1 and EMT-2 implementation), because the full frame was acquired at such a low rate (345 Hz) that a great number of laser pulses entered the same acquisition window. Furthermore, even setting F_F to the maximum value for the smallest window (e.g., for laser transmission event recording and experimental PRF determination), we had to accept a large error probability. In this case, in fact, the relatively large variance of T_F did not allow optimisation of P_{err}. Therefore, for the two test sessions F_F was initially set to the values:

- F_{F_10} = 19.5 Hz in full frame with f = 10 Hz (ELOP-PLD);
- F_{F_20} = 39.5 Hz in full frame with f = 20 Hz (ELOP-PLD); and
- F_{F_40k} = 38 kHz in smallest window with f = 40 kHz (LOAS).

The key parameter used for evaluating the performance of the Phoenix NIR camera was the Percentage of Acquired Pulses (%AP) with respect to the total number of laser pulses transmitted in a certain Pulse Train Duration (PTD). Results relative to the NIR camera tests performed with the ELOP-PLD system are presented in Table 8-3.

Table 8-3: Phoenix NIR Camera F_F Tests Results (f = 10 Hz and 20 Hz)

ELOP-PLD Parameters			PHOENIX NIR	
PRF	PTD	τ	F_F	%AP
10 Hz	10 s	19 ns	19.5 Hz	67%
	30 s	19 ns	19.5 Hz	62%
	60 s	19 ns	19.5 Hz	71%
	120 s	19 ns	19.5 Hz	65%
20 Hz	10 s	19 ns	39.5 Hz	63%
	30 s	19 ns	39.5 Hz	68%
	60 s	19 ns	39.5 Hz	52%
	120 s	19 ns	39.5 Hz	58%

Results relative to the Phoenix NIR camera tests performed with the LOAS system are presented in Table 8-4.

Table 8-4: Phoenix NIR Camera F_F Tests Results (f = 40 kHz)

ELOP-PLD Parameters			PHOENIX NIR	
PRF	PTD	τ	F_F	%AP
40 kHz	10 s	5 ns	38 kHz	17%
	30 s	5 ns	38 kHz	12%
	60 s	5 ns	38 kHz	19%
	120 s	5 ns	38 kHz	18%

8.2.3.4 Determination of DAS Memory Requirements

The Phoenix NIR camera Digital Acquisition System (DAS), employed at the PILASTER STU, was based on commercial PC technology. Therefore, before performing ground and flight experimental activities, it was essential to define the DAS memory required for recording the digital frames acquired by the NIR camera during representative test/training missions. The duration (D) of typical test/training recording sessions was identified between 10 and 120 seconds. The maximum frame rate of the Phoenix NIR camera

(with DAS) is 38 kHz. Each frame is composed by R = 320 × 256 pixels, and each frame occupies memory 14 bits (grey scale images). Therefore, in the absence of any data compression and neglecting the few bits introduced by the IMAGE-PRO PLUS imaging software, the data flow from the camera to the PC, considering a typical 5% incidence of the communication flag bits, we obtain:

$$F_{data} = F_F \cdot R \cdot 14 \cdot 1.05 \ \ bit/sec \tag{8.39}$$

The memory required for acquisition is given by:

$$M = \frac{D \cdot F_{data}}{8} \ \ Byte \tag{8.40}$$

For instance, for D = 120 secs and F_F = 39.5 Hz (e.g., optimal F_F for ELOP-PLD in Band N° 2), considering a full frame data acquisition, we obtain:

$$M = \frac{120 \ \ \sec \cdot 47.6 \ \ Mbit/\sec}{8} \cong 713.50 \ MByte \tag{8.41}$$

Considering a 38 kHz data acquisition in smallest window (R = 2 × 128 pixels), assuming D = 120 secs, we obtain:

$$M = \frac{120 \ \ \sec \cdot 143 \ \ Mbit/\sec}{8} \cong 2.15 \ GByte \tag{8.42}$$

A graph showing the DAS memory requirements as a function of mission duration, for various representative frame rates, is shown in Figure 8-20. Therefore, as the DAS memory requirements were fulfilled by commercial technology, a standard 40 *GByte* PC hard-disk was installed in the Phoenix DAS computer.

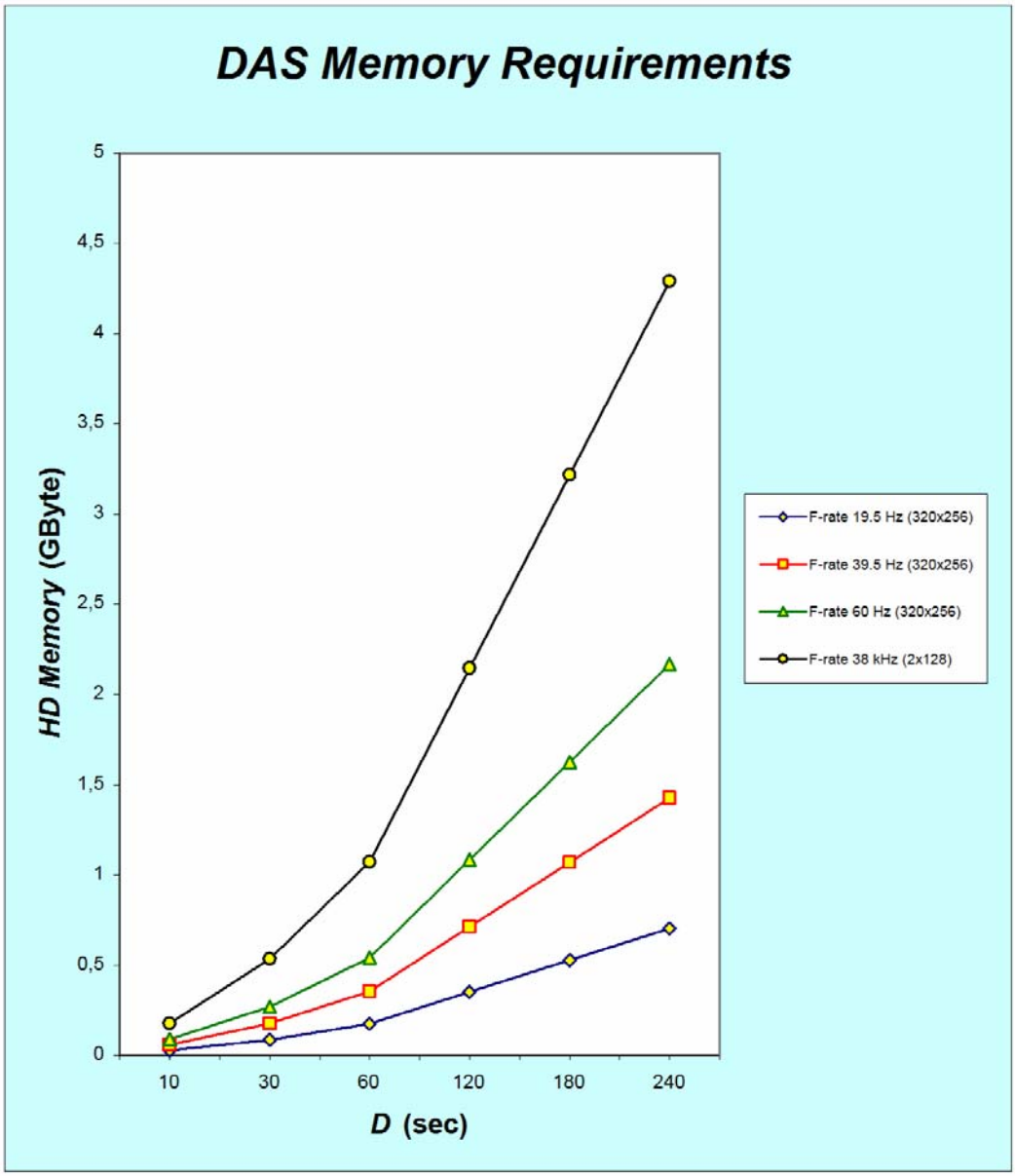

Figure 8-20: DAS Computer Hard-Disk Memory Requirements.

8.2.4 EMT-CT Sessions at $\lambda = 1064$ nm

Using the ELOP PLD system, operating at $\lambda = 1064$ nm, preliminary ground tests were performed using the EMT-CT. Particularly, the laser source (ELOP-PLD) and the NIR camera were placed very close to the target surface (i.e., 100 m and 80 m respectively) in a day with very good visibility ($V = 34$ km) and low humidity ($RH = 41\%$ at $T = 15°C$). During the experiment with this control technique, the PLD laser was activated 10 times for periods of 30 seconds. For each test session, a minimum of 25 spot images were recorded (and at least 2 PEP readings for each spot image). The maximum and minimum differences (ε_{max} and εmin) observed between the energy values obtained using EMT-1/EMT-2 and the PLD output energy are reported in Table 8-5.

Table 8-5: Differences between PLD Output and PILASTER Measurements

Session	EMT-1		EMT-2	
	ε_{max}	ε_{min}	ε_{max}	ε_{min}
1	-27.12%	-12.51%	-11.03%	-4.86%
2	-19.34%	**-7.34%**	-10.47%	-5.12%
3	-28.06%	-18.64%	-13.95%	-6.65%
4	-33.24%	-15.04%	**-14.76%**	-10.23%
5	-28.29%	-19.12%	-12.79%	-8.49%
6	-18.02%	-10.27%	-9.87%	**-4.22%**
7	-21.13%	-18.35%	-13.57%	-9.43%
8	-15.90%	-11.67%	-11.70%	-7.42%
9	**-34.69%**	-8.78%	-9.07%	-6.43%
10	-27.42%	-10.18%	-8.48%	-5.54%

Both EMT-1 and EMT-2 gave under estimated values of the incident spot energy (i.e., a negative systematic error). In many cases EMT-1 could only provide rough estimations of the laser spot energy, with significant discrepancies between the various test sessions (i.e., -34.69% maximum and -7.34% minimum errors). On the other hand, using EMT-2 the error never exceeded -14.76% with an observed minimum error of -4.22%. These errors were due to sensors detection thresholds, loss of some spot fringes in the NIR images due to background noise, and other systematic or random errors affecting both techniques EMT-1/EMT-2 and the EMT-CT itself.

Cumulating the experimental data relative to the various test sessions, two samples of 300 error measurements were formed, relative to the EMT-1 and EMT-2 errors. These data were statistically analysed in order to determine corrections for the measurements performed using the two techniques. The normality of the data samples was verified using standard statistical techniques (i.e., χ^2 tests). The values of mean and standard deviation calculated for the error samples (s) and the 95% confidence intervals (CI) for the mean (μ) and standard deviations (σ) calculated for the corresponding normal populations are reported in Table 8-6. The 95% CI for μ and σ were calculated as follows:

$$\bar{x} - 1.96\,\frac{s}{\sqrt{n-1}} < \mu < \bar{x} + 1.96\,\frac{s}{\sqrt{n-1}} \tag{8.43}$$

$$\frac{s}{\left[1+\left(\frac{1.96}{\sqrt{2n}}\right)\right]} < \sigma < \frac{s}{\left[1-\left(\frac{1.96}{\sqrt{2n}}\right)\right]} \tag{8.44}$$

Table 8-6: Results of Errors Statistical Analysis for EMT-1 and EMT-2

	EMT-1		EMT-2	
	Mean (%)	SD (%)	Mean (%)	SD (%)
Sample	$\bar{x}_1 = -17{,}57$	$s_1 = 3{,}54$	$\bar{x}_2 = -9{,}29$	$s_2 = 2{,}47$
Pop. 95% CI	$-18.06 < \mu < -17.08$	$3.28 < \sigma < 3.85$	$-9.57 < \mu < -9.01$	$2.29 < \sigma < 2.68$

Figure 8-21 shows the Probability Density Functions (PDF) obtained from the experimental data.

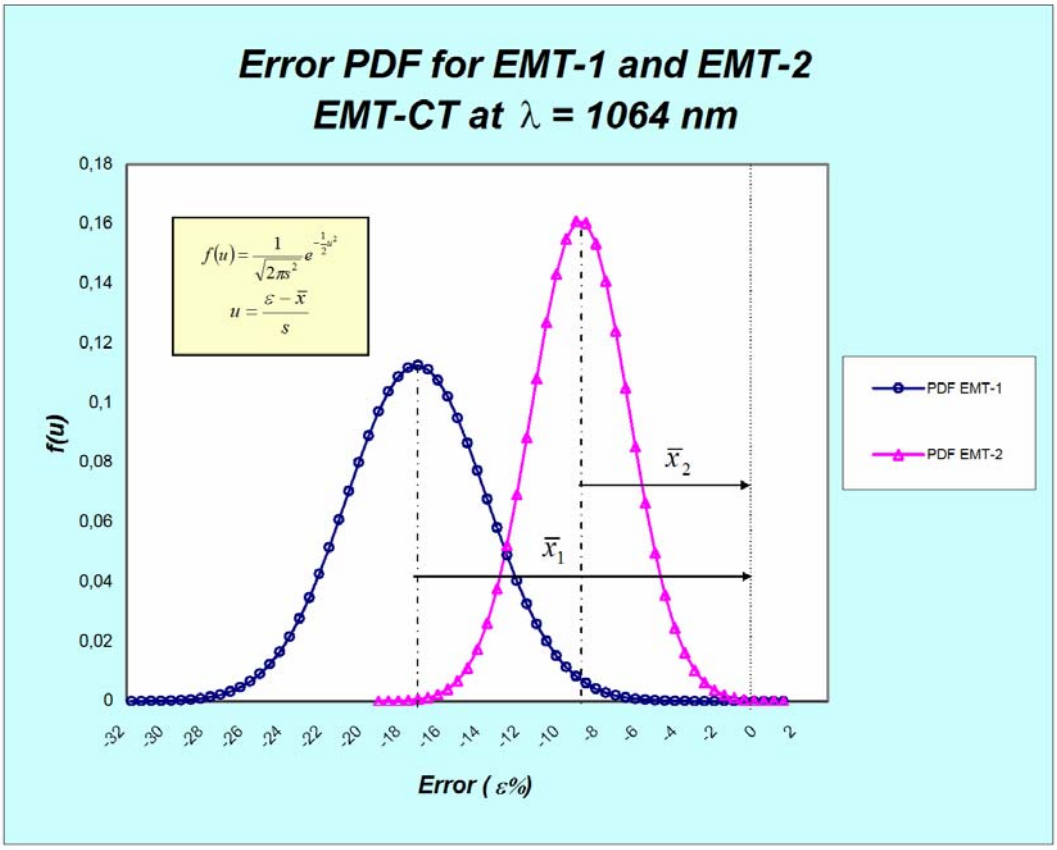

Figure 8-21: Error PDF for EMT-1 and EMT-2.

Using these results, it was possible to improve the reliability of the two techniques. This was done by applying a correction factor in the transformation from the NIR camera grey scale Pixel Intensity Matrix (PIM) to the corresponding Energy Intensity Matrix (EIM). The correction factors C_1 and C_2 (for EMT-1 and EMT-2 respectively) were:

$$C_1 = 1 + |\bar{x}_1| = 1.1757 \tag{8.45}$$

$$C_2 = 1 + |\bar{x}_2| = 1.0929 \tag{8.46}$$

The ELOP-PLD factory data gave a Probable Error (PE_{PLD}) of ±4% for the system energy output due to instability, aging, etc. (i.e., 130 mJ ±4%). Considering the results of our analysis, since $PE = 0.6745 \cdot \sigma$, we obtained $PE_1 = \pm 2.39\%$ and $PE_2 = \pm 1.67\%$ for EMT-1 and EMT-2 respectively. Therefore, accumulating the errors, the PE of the measurements performed using the two techniques (PE_{M1}, PE_{M2}) were the following:

$$PE_{M1} = \sqrt{PE_{PLD}^{\ 2} + PE_1^{\ 2}} = \pm 4.66\% \tag{8.47}$$

$$PE_{M2} = \sqrt{PE_{PLD}^{\ 2} + PE_2^{\ 2}} = \pm 4.33\% \tag{8.48}$$

8.2.5 Propagation Trials Results

After the initial test phase devoted to PILASTER measurement techniques verification and optimisation, actual extinction measurement trials were performed at the PILASTER range using EMT-1/EMT-2 for λ = 1064 nm (ELOP-PLD) and EMT-3 for λ = 1550 nm (LOAS). Most of the test activities were carried out during fall, spring and summer in the years 2002 and 2003. Propagation tests at λ = 1064 nm were performed in dry weather conditions, while tests at λ = 1550 nm were performed in both dry and rainy weather conditions. Test conditions and results are presented below.

8.2.5.1 Propagation Trials at λ = 1064 nm

Propagation trials at λ = 1064 nm were performed using the PILASTER modular target located at the *Casa Marongiu* site and the ELOP-PLD laser system positioned along the target normal at a distance of 2.5 km, 4 km and 5.5 km. The target Mean Sea Level (MSL) altitude was about 500 m and the maximum altitude difference between the laser transmitter and the target was about 140 m at a distance of 5.5 km. The geometry of the λ = 1064 nm propagation tests performed at the PILASTER range are shown in Figure 8-22. Table 8-7 shows the relevant data describing the meteorological conditions in which the atmospheric propagation measurements were performed (dry-air conditions). The various test cases have been grouped for classes of visibility and the corresponding International Visibility Code (IVC) classes are reported. When significant variations of T and/or RH were observed during the measurements, only the average values calculated in the relevant time intervals have been reported. The prevailing wind direction/ intensity during the measurements is listed with respect to the laser to target slant-path (usual counter-clockwise convention). The values of the Turbulence Structure Constant (C_n) were determined using the *Scintec* BLS900 laser scintillometer, with a measurement baseline of 5 km between transmitter and receiver (along the target normal).

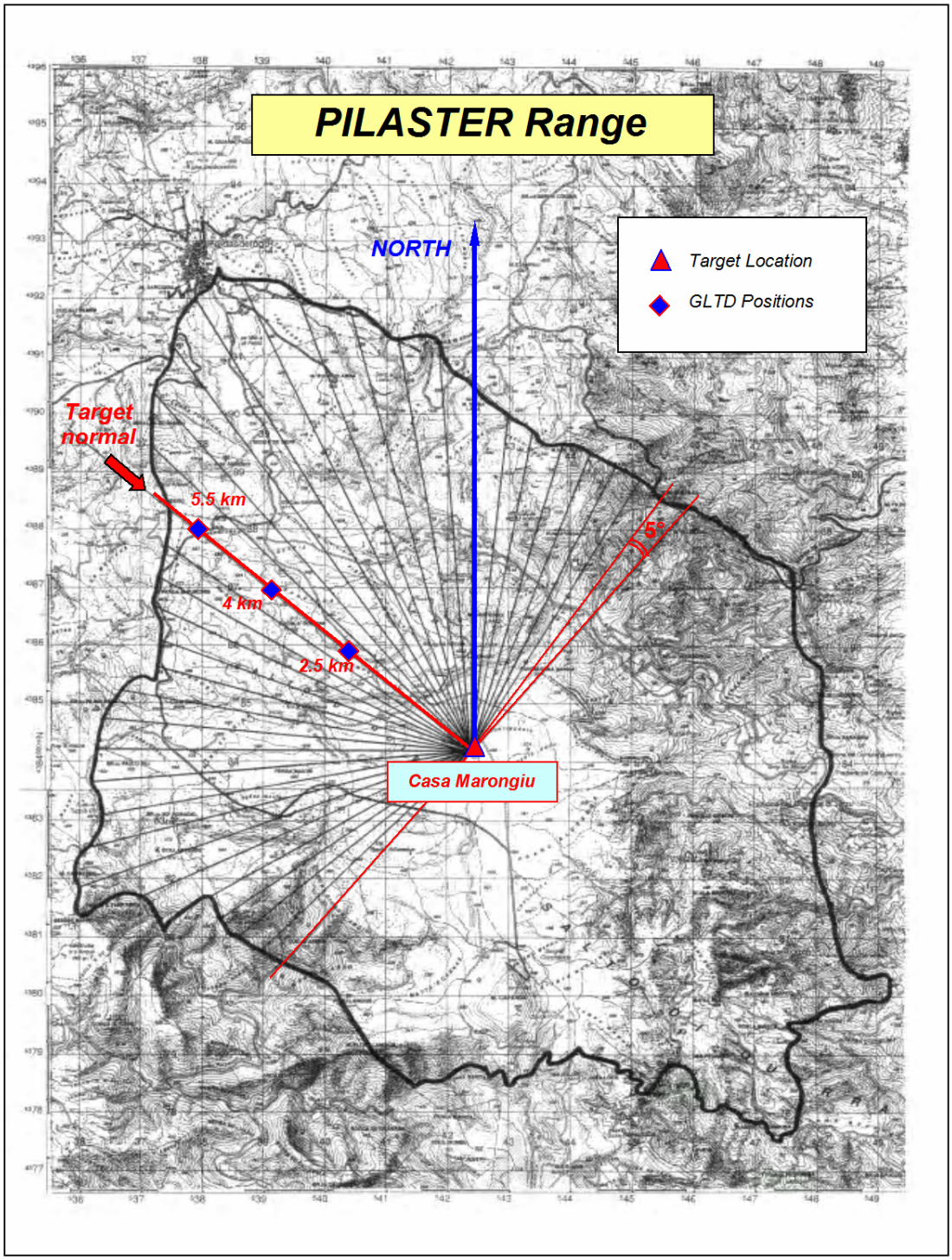

Figure 8-22: Geometry of Atmospheric Propagation Measurements at λ = 1064 nm.

Table 8-7: Meteorological Data for Dry-Air Propagation Measurements at λ = 1064 nm

Group	Case	V (km)	RH (%)	T (°C)	C_n	Cloud	Wind (°/kts)	IVC
I	A	2.5	82	24	$6.77*10^{-8}$	6/8	0/0	Haze
	B	3.0	85	15	$1.80*10^{-8}$	5/8	0/0	
	C	3.5	76	23	$9.86*10^{-7}$	7/8	92/2	
II	A	5	73	25	$8.79*10^{-8}$	3/8	0/0	Light Haze
	B	6.0	66	27	$6.67*10^{-8}$	4/8	237/3	
	C	7.0	68	7	$1.82*10^{-7}$	7/8	0/0	
III	A	8.0	67	24	$8.96*10^{-8}$	3/8	0/0	
	B	8.5	58	28	$6.70*10^{-8}$	3/8	120/5	
	C	9.0	64	30	$2.92*10^{-7}$	4/8	0/0	
IV	A	10.0	51	20	$7.16*10^{-7}$	2/8	40/6	Clear
	B	10.5	58	28	$1.87*10^{-7}$	1/8	95/12	
	C	11	51	18	$6.39*10^{-8}$	2/8	120/8	
	D	12.5	48	32	$8.56*10^{-7}$	3/8	0/0	
V	A	14.5	52	18	$1.09*10^{-8}$	2/8	22/4	
	B	15.0	44	32	$4.87*10^{-7}$	3/8	320/7	
	C	18.5	56	24	$7.98*10^{-8}$	0/8	35/5	
VI	A	20.5	40	31	$4.49*10^{-8}$	0/8	0/0	Very Clear
	B	22.5	41	35	$5.87*10^{-7}$	2/8	25/8	
	C	25.0	47	35	$7.56*10^{-7}$	1/8	125/10	
	D	34.0	35	32	$6.84*10^{-8}$	0/8	15/7	

For each case listed in Table 8-7, a minimum of 25 energy measurements were performed (samples of 25 to 50 laser spot measurements were used) using at least two of the ELOP-PLD locations shown in Figure 8-22. Dry-air extinction tests were performed in all meteorological conditions listed in Table 8-7 only with a system to target slant-range (SR) of 2.5 km. With SR = 4 km and SR = 5.5 km, extinction tests were performed in a representative sub-set of dry-air meteorological conditions. Rain extinction tests were not performed at λ = 1064 nm.

Transmittance and extinction coefficient values relative to the various test cases (i.e., meteorological conditions listed in Table 8-7), calculated using the ESLM model with SR = 1 km, are listed in Table 8-8.

Table 8-8: Calculated Extinction Coefficients for Dry-Air Conditions (SR = 2.5 km)

Group	Case	IVC Categ.	Model τ	Model γ (km^{-1})
I	A	Haze	0.077	1.025
	B		0.127	0,824
	C		0.168	0,714
II	A	Light Haze	0.287	0,500
	B		0.351	0,419
	C		0.448	0,321
III	A		0.455	0,315
	B		0.470	0,302
	C		0.476	0,297
IV	A	Clear	0.549	0,240
	B		0.532	0,252
	C		0.583	0,216
	D		0.575	0,221
V	A		0.652	0,171
	B		0.622	0,190
	C		0.675	0,157
VI	A	Very Clear	0.688	0,149
	B		0.684	0,152
	C		0.687	0,150
	D		0.755	0,112

The extinction coefficients in Table 8-8 were computed from ESLM model transmittances, using the simple equation:

$$\gamma = -\frac{ln\,\tau}{SR} \tag{8.49}$$

However, it is important to observe that, although the ESLM model provides independent estimates of both absorptive transmittance (τ_{ai}) and scattering transmittance (τ_{si}), only the scattering contribution to the extinction coefficient (γ_{si}) is independent of range. We should remember, in fact, that the total precipitable water in mm is $w = SR \cdot AH$ (where SR is the slant-range in km and AH is the absolute humidity in g/m^3), and AH is approximated by:

$$AH = 1322.8\frac{RH}{T}exp\left[\frac{25.22(T-273.16)}{T} - 5.31ln\left(\frac{T}{273.16}\right)\right] \tag{8.50}$$

According to the ESLM model, as $w < 54$ in all cases listed in Table 8-7, the ESLM absorptive transmittance is given by:

$$\tau_{ai} = e^{-0.0363\cdot\sqrt{w}} \tag{8.51}$$

Therefore, in this case, the absorptive extinction coefficient (γ_{ai}) is given by:

$$\gamma_{ai} = 0.0363 \cdot AH \cdot \frac{1}{\sqrt{SR}} \tag{8.52}$$

where the SR dependency of γ_{ai} is evident (obviously, for SR = 1 km the model γ_{ai} becomes a function of *AH* only). For instance, with *SR* = 10 km, the model γ_{ai} is about one third of the value calculated, with the same *RH* and *T* conditions, with SR = 1 km. In other words, the ESLM empirical model implies a range dependency of the extinction coefficient, which prevents a direct comparisons of the experimental γ values found at a certain SR with γ values predicted or measured at a different SR. Although this appears as a limitation of the ESLM model for practical applications, for all SR considered we determined τ from NIR-camera energy measurements and γ using equation (8.34), and compared the calculated values with the experimental results. Therefore, for each SR, different sets of corrections were computed simply by comparing the predicted ESLM τ and γ values with the experimental data.

Since the initial phases of the test activity, data collected in various meteorological conditions and with various laser slant-paths, demonstrated moderate discrepancies between the extinction measurements performed with EMT-1 and EMT-2 (i.e., 8% maximum difference, after EIM correction with C_1 and C_2). Furthermore, using the two techniques, no significant correlation was observed between the differences in the measurements and the lengths of the laser slant-paths used to gather the experimental data. Table 8-9 shows the results of transmittance measurements performed using the EMT-2 technique for a laser slant-path of 2.5 km, compared with ESLM model computations.

Table 8-9: Transmittance Data and ESLM Model Corrections (λ = 1064 nm – SR = 2.5 km)

Group	Case	IVC Categ.	Experim. τ	Model τ	Error (%)	Group Corr.	IVC Cat. Corr.
I	A	Haze	0.088	0.077	14.91	1.149	1.149
	B		0.146	0.127	15.15		
	C		0.192	0.168	14.57		
II	A	Light Haze	0.331	0.287	15.46	1.150	1.141
	B		0.406	0.351	15.69		
	C		0.510	0.448	13.80		
III	A		0.513	0.455	12.80	1.131	
	B		0.537	0.470	14.20		
	C		0.535	0.476	12.40		
IV	A	Clear	0.630	0.549	14.58	1.140	1.132
	B		0.597	0.532	12.17		
	C		0.666	0.583	14.23		
	D		0.662	0.575	15.14		
V	A		0.737	0.652	13.00	1.125	
	B		0.704	0.622	13.20		
	C		0.751	0.675	11.20		
VI	A	Very Clear	0.765	0.688	11.14	1.113	1.113
	B		0.767	0.684	12.16		
	C		0.760	0.687	10.52		
	D		0.840	0.755	11.27		

In all cases, the measured transmittance values (i.e., average of 25 – 50 spot measurements) were greater than the values computed using the ESLM model. The observed differences between measured and ESLM transmittances varied between 10.52% and 16.64%. The ESLM transmittance model corrections computed for each group and for each IVC category are also listed in Table 8-9. It is evident, looking at the results in Table 8-9 and at their graphical representation in Figure 8-23, that the difference between predicted and measured transmittance decreases significantly as atmospheric visibility increases.

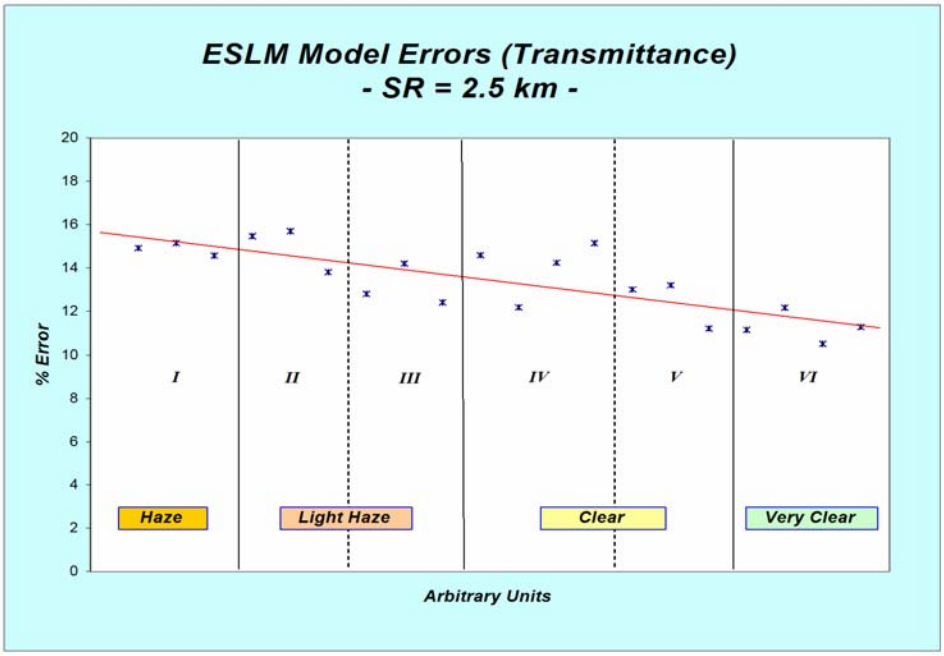

Figure 8-23: ESLM Model Errors (Transmittance) for SR = 2.5 km.

Table 8-10 presents the same results (SR = 2.5 km) in terms of extinction coefficient.

Table 8-10: Extinc. Coeff. Data and ESLM Model Corrections (λ = 1064 nm – SR = 2.5 km)

Group	Case	IVC Categ.	Experim. γ (km^{-1})	Model γ (km^{-1})	Error (%)	Group Corr.	IVC Cat. Corr.
I	A	Haze	0.967	1,025	-5.64	0.923	0.923
	B		0.757	0,824	-8.09		
	C		0.647	0,714	-9.34		
II	A	Light Haze	0.437	0,500	-12.62	0.857	0.846
	B		0.360	0,419	-14.15		
	C		0.269	0,321	-16.10		
III	A		0.265	0,315	-15.99	0.836	
	B		0.249	0,302	-17.59		
	C		0.250	0,297	-15.75		
IV	A	Clear	0.186	0,240	-22.70	0.772	0.750
	B		0.207	0,252	-18.20		
	C		0.163	0,216	-24.66		
	D		0.165	0,221	-25.47		
V	A		0.122	0,171	-28.57	0.728	
	B		0.140	0,190	-26.11		
	C		0.115	0,157	-27.01		
VI	A	Very Clear	0.107	0,149	-28.24	0.692	0.692
	B		0.106	0,152	-30.21		
	C		0.110	0,150	-26.64		
	D		0.070	0,112	-37.99		

Experimental data and error computations relative to the measurements performed with SR = 4 km and SR = 5.5 km are presented in Table 8-11 to Table 8-14. Although measurements with these SRs were not performed in all meteorological conditions listed in Table 8-7, looking at the available data it appears evident that the ESLM model errors, both for transmittance and extinction coefficient calculations, are comparable with the errors computed for SR = 2.5 km.

Table 8-11: Transmittance Data and ESLM Model Corrections (λ = 1064 nm – SR = 4 km)

Group	Case	IVC Categ.	Experim. τ	Model τ	Error (%)	Group Corr.	IVC Cat. Corr.
II	A	Light Haze	0.179	0.147	17.88	1.214	1.213
	C		0.351	0.290	17.39		
III	B		0.384	0.323	15.92	1.212	
	C		0.410	0.332	18.96		
IV	A	Clear	0.489	0.406	17.03	1.192	1.168
	B		0.463	0.393	15.18		
V	C		0.652	0.570	12.52	1.143	
VI	A	Very Clear	0.681	0.590	13.34	1.154	1.154

Table 8-12: Transmittance Data and ESLM Model Corrections (λ = 1064 nm – SR = 5.5 km)

Group	Case	IVC Categ.	Experim. τ	Model τ	Error (%)	Group Corr.	IVC Cat. Corr.
II	B	Light Haze	0.143	0.118	20.78	1.252	1.280
	C		0.233	0.188	19.48		
III	B		0.285	0.224	21.48	1.308	
	C		0.314	0.234	25.45		
IV	A	Clear	0.381	0.303	20.42	1.259	1.255
	B		0.371	0.294	20.69		
V	A		0.537	0.439	18.30	1.252	
	B		0.527	0.412	21.82		
VI	B	Very Clear	0.611	0.512	16.18	1.181	1.181
	D		0.726	0.621	14.41		

Table 8-13: Extinc. Coeff. Data and ESLM Model Corrections (λ = 1064 nm – SR = 4 km)

Group	Case	IVC Categ.	Experim. γ	Model γ	Error (%)	Group Corr.	IVC Cat. Corr.
II	A	Light Haze	0.430	0.480	-10.40	0.872	0.849
	C		0.262	0.309	-15.30		
III	B		0.239	0.283	-15.48	0.827	
	C		0.223	0.276	-19.17		
IV	A	Clear	0.179	0.225	-20.59	0.810	0.787
	B		0.192	0.233	-17.45		
V	C		0.107	0.140	-23.50	0.765	
VI	A	Very Clear	0.096	0.132	-27.19	0.728	0.728

Table 8-14: Extinc. Coeff. Data and ESLM Model Corrections (λ = 1064 nm – SR = 5.5 km)

Group	Case	IVC Categ.	Experim. γ	Model γ	Error (%)	Group Corr.	IVC Cat. Corr.
II	B	Light Haze	0.346	0.388	-10.80	0.881	0.850
	C		0.264	0.304	-13.00		
III	B		0.228	0.272	-16.16	0.818	
	C		0.211	0.264	-20.20		
IV	A	Clear	0.176	0.217	-19.09	0.809	0.774
	B		0.178	0.223	-19.29		
V	A		0.113	0.150	-24.71	0.738	
	B		0.116	0.161	-27.66		
VI	B	Very Clear	0.090	0.122	-26.53	0.703	0.703
	D		0.058	0.087	-32.95		

The ESLM model errors for computing γ, relative to the various test cases are shown in Figure 8-24. The error trends were not significantly affected by the system to target SR and, in all cases, the ESLM model always over-estimated the extinction coefficient (i.e., under-estimated transmittance). Therefore, the experimental results are not in contrast with the $1/\sqrt{SR}$ dependency of γ_{ai} implied in the ESLM empirical model. The under estimation of τ can be explained observing that the ESLM model is a two components model (i.e., scattering transmittance τ_{si} and absorptive transmittance τ_{ai}) whose empiric equations were derived from independent scattering and absorption measurements, in which either absorption or scattering were neglected due to the particular test conditions. On the other hand, the effects of turbulence and other linear and non-linear propagation phenomena not included in the ESLM model, did not seem to significantly affect the energy measurements performed using EMT-2 and the ELOP-PLD laser system in the specified test conditions.

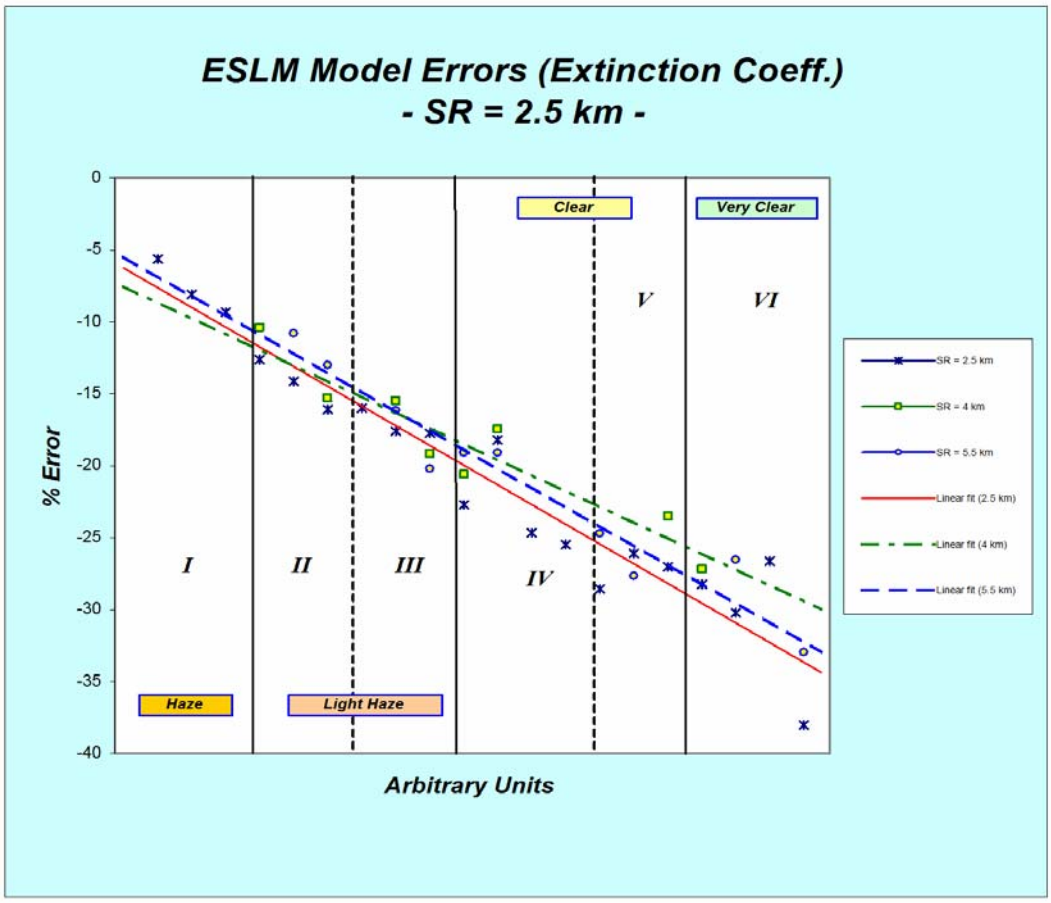

Figure 8-24: ESLM Model Errors for Computation of γ (λ = 1064 nm – SR = 2.5 km).

8.2.5.2 Propagation Tests at λ = 1550 nm

Propagation tests at λ = 1550 nm were performed using EMT-3, with the geometry illustrated in Figure 8-7. The parameters describing the meteorological conditions during the tests are listed in the Table 8-15 and Table 8-16.

Table 8-15: Meteorological Data for Dry-Air Propagation Measurements at λ = 1550 nm

Group	Case	V (km)	RH (%)	T (°C)	C_n	Cloud	Wind (°/kts)	IVC
1	a	3.0	82	25	$7.45*10^{-8}$	5/8	92/8	Haze
	b	4.0	85	21	$4.49*10^{-8}$	3/8	95/2	
2	a	7.0	78	22	$5.27*10^{-8}$	5/8	0/0	Light Haze
	b	8.0	67	25	$7.30*10^{-7}$	2/8	120/5	
	c	9.0	72	29	$2.65*10^{-8}$	4/8	45/8	
3	a	12.0	61	23	$3.15*10^{-8}$	3/8	0/0	Clear
	b	15.5	49	31	$5.90*10^{-8}$	0/8	0/0	
	c	18.0	55	28	$7.66*10^{-7}$	0/8	70/2	
	d	20.0	57	30	$5.23*10^{-7}$	2/8	54/11	
4	a	22.5	52	31	$5.80*10^{-7}$	0/8	0/0	Very Clear
	b	24.0	44	35	$4.65*10^{-7}$	0/8	130/6	
	c	28.0	57	35	$6.40*10^{-8}$	2/8	46/7	

Table 8-16: Meteorological Data for Propagation Measurements with Rain at λ = 1550 nm

Group	Case	V (km)	RH (%)	T (°C)	C_n	Wind (°/kts)	Rainfall (cm/hr)	Type of Rain
5	a	3.0	100	10	$3.22*10^{-7}$	23/4	2.10	Heavy rain
	b	5.0	90	12	$5.90*10^{-7}$	122/10	1.45	Med. Rain
	c	6.0	90	18	$8.12*10^{-8}$	15/5	0.30	Light rain

The extinction coefficients calculated, for each case listed in the Table 8-15 and Table 8-16, using the ESLM model, are listed in the Tables 8-17 and 8-18.

Table 8-17: Calculated Extinction Coefficients for Dry-Air

Group	Case	IVC	Model γ (km^{-1})
1	a	Haze	1.082
	b		0.890
2	a	Light Haze	0.689
	b		0.661
	c		0.671
3	a	Clear	0.573
	b		0.572
	c		0.556
	d		0.565
4	a	Very Clear	0.555
	b		0.556
	c		0.579

Table 8-18: Calculated Extinction Coefficients for Rain

Group	Case	Type of Rain	Model γ (km^{-1})
5	a	Heavy rain	2.944
	b	Med. rain	2,429
	c	Light rain	1,231

The ESLM extinction coefficients in the Table 8-17 and Table 8-18 were computed from model transmittances using the equation $\gamma = -ln\,\tau/SR$ with SR = 1 km. Experimental data and ESLM model errors relative to the measurements performed in both dry and rainy conditions are presented in the Table 8-19 and Table 8-20.

Table 8-19: Dry-Air Experimental Data and ESLM Model Corrections (λ = 1550 nm)

Group	Case	IVC	Model γ	Exper. γ	Error %	Case Corr.	IVC Cat. Corr.
1	a	Haze	1.082	0.816	-24.56	0.754	0.745
	b		0.890	0.655	-26.43	0.736	
2	a	Light Haze	0.689	0.446	-35,20	0.648	0.647
	b		0.661	0.479	-27,58	0.724	
	c		0.671	0.381	-43,27	0.567	
3	a	Clear	0.573	0.332	-42,10	0.579	0.584
	b		0.572	0.382	-33,30	0.667	
	c		0.556	0.350	-37,10	0.629	
	d		0.565	0.261	-53,80	0.462	
4	a	Very Clear	0.555	0.324	-41,60	0.584	0.601
	b		0.556	0.354	-36,30	0.637	
	c		0.579	0.337	-41,67	0.583	

Table 8-20: Rain Experimental Data and ESLM Model Corrections (λ = 1550 nm)

Group	Case	Type of Rain	Model γ	Exper. γ	Error %	Case Corr.
5	a	Heavy rain	2.596	2.266	-12.70	0.873
	b	Med. rain	2.080	2.006	-3.56	0.964
	C	Light rain	0.864	0.729	-15.67	0.843

It is evident that, also at λ = 1550 nm, there is a considerable difference between the experimental data and the ESLM model results. Again, the over estimation of γ can be explained observing that the ESLM model is a two components model whose empiric equations were derived from independent scattering and absorption measurements, in which either absorption or scattering were neglected due to the particular test conditions.

Furthermore, as the ESLM model uses different sets of equations for modelling absorption at λ = 1064 nm and λ = 1550 nm, and slightly different parameters in the equations for modelling atmospheric scattering at the two wavelengths, remarkable differences were observed between the results obtained at λ = 1064 nm and λ = 1550 nm. The differences in the overall (scattering plus absorption) transmittances and extinction coefficients, computed for a transmission path of 1 km and the same set of meteorological parameters listed in Table 8-15 (dry-air), are shown in Figure 8-25. The greater contribution to the observed differences was due to absorptive extinction, which for λ = 1550 nm and $w > 1.1$, was modelled as:

$$\gamma_{ai} = -\frac{ln\left(0.802 \cdot \frac{1.1}{w}\right)^{0.111}}{SR} \tag{8.53}$$

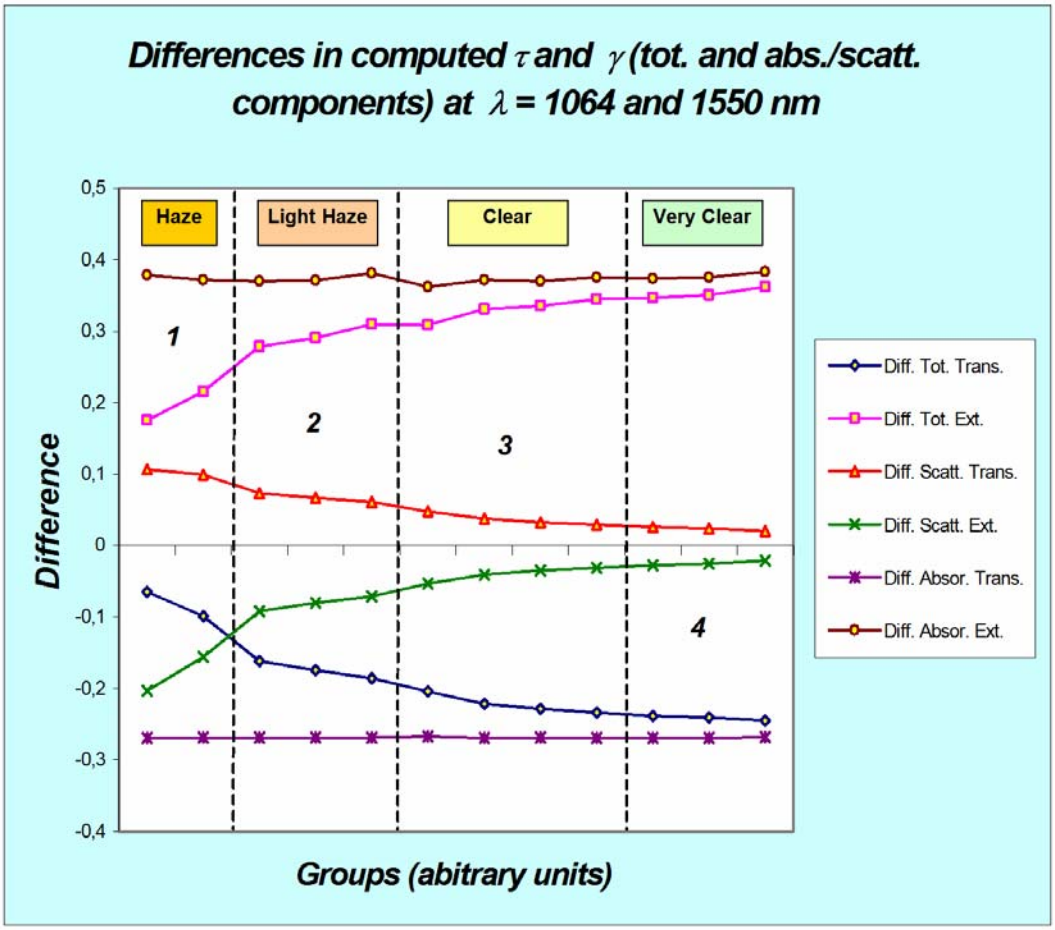

Figure 8-25: Differences in τ and γ (Total and Absorptive/Scattering Components) Computed with the ESLM Model for λ = 1064 nm and λ = 1550 nm.

On the other hand, the ESLM model for rainy conditions (modified using the LOWTRAN equation for estimating the scattering coefficient), fitted reasonably well the experimental data, with transmittance computation errors not exceeding 15.67% (light rain case).

8.2.5.3 Laser Propagation Data Base

Although the PILASTER Laser Propagation Data Base (LPDB) is at the initial stages of its compilation, and the quantity of experimental data collected is limited at the moment, current and future activities performed at the PILASTER range are expected to produce sufficient data to compute accurate correction factors required to increase the reliability of the propagation models used for simulation, mission planning and system performance analysis purposes.

With reference to the ESLM empirical model, the correction factors to the model presented above were computed by comparing measured and calculated transmittance/extinction values obtained from atmospheric visibility, relative humidity and temperature observations. Particularly, all experimental data (i.e., spot energy measurements) collected for each group-case were cumulated, and only results relative to the average energy measurements were presented in the various tables. Adopting this approach, it is evident that some information was lost in the process (i.e., the fluctuations experienced by the measured laser spot energies and the consequent variations of the errors/corrections computed for each spot measurement in all samples considered). It is believed that a statistical approach, making use of the LPDB,

would be well suited for a progressive refinement of the atmospheric model corrections. As an example, the Atmospheric Model Correction Functions (AMCFs) relative to the tests performed in dry weather at λ = 1064 nm are shown in Figure 8-26.

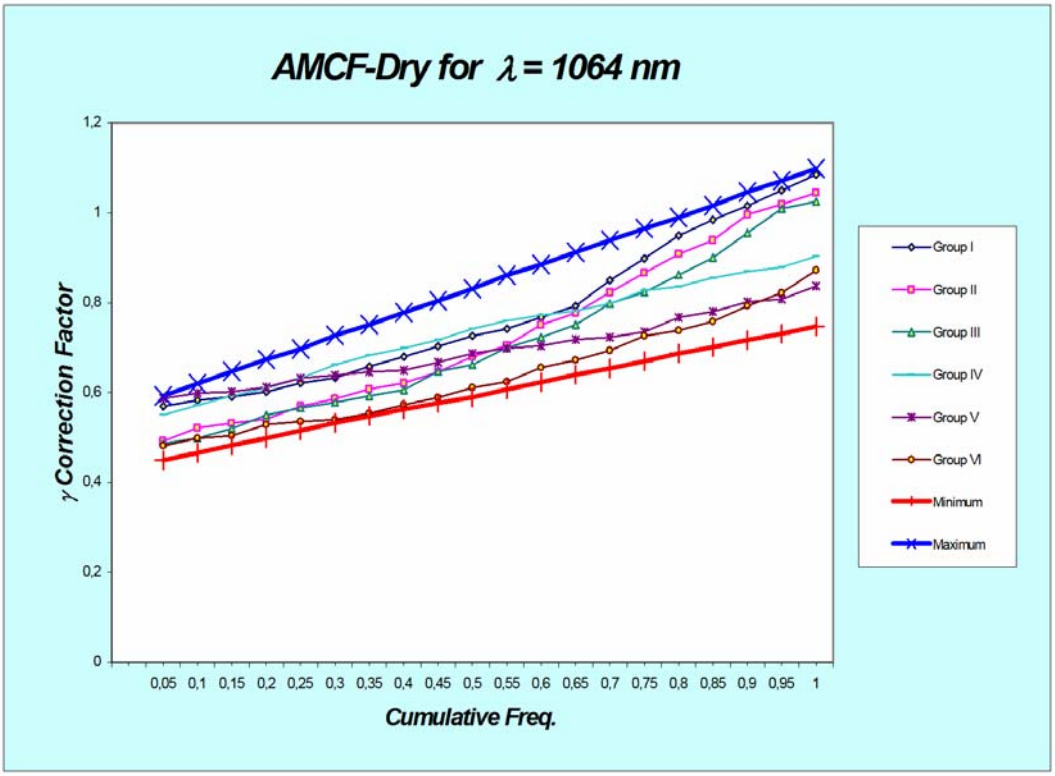

Figure 8-26: Correction Functions for ESLM-Dry γ Computations with λ = 1064 nm.

The lines denoted "Minimum" and "Maximum" in the graph, represent the lower and upper bounds of all AMCFs. The equations fitting these lines are the following:

$$Minimum \rightarrow y = 0.3123x + 0.4344 \quad (8.54)$$

$$Maximum \rightarrow y = 1.8812x + 1.0656 \quad (8.55)$$

Depending on the specific application, these equations can be used to determine corrections for the atmospheric propagation factors computed using the ESLM model. For instance, eq. (8.39) can be used in eye-safety studies, where a lower bound approximation for the computed atmospheric extinction is to be considered acceptable, while eq. (8.40) is most convenient for applications like range performance prediction and simulation studies for the operational employment of laser guided weapons, where an upper bound approximation is preferable.

It is important to note that an essential pre-requisite to this approach is the definition of a probability level which is adequate for the specific application. In most safety studies for test/training operations at the ranges a 100% probability would be adopted, while for the majority of operational mission planning tasks (e.g., range performance calculations and 'spiker' aircraft mission profile optimisation) a lower probability level may be accepted (e.g., 50 – 80%), depending on the operational needs and the geometric constraints of the mission (target 'lethal range', aircraft/systems limitations, time constraints, etc.).

8.2.6 LRF/LTD Systems Pointing Accuracy

Using the LTM-STU instrumentation, the pointing accuracy of various ground LRF/LTD systems (for FAC operations) was determined. The tests were performed using the PILASTER modular target and STU instrumentation. The tested Nd:YAG LRF/LTD systems were the following:

- ELOP (Electro-optics Industries Ltd) PLD;
- LITTON (Litton Systems Inc.) GLTD; and
- CILAS (Compagnie Industrielle de Lasers) G3.

The measurements were performed with the 3 LRF/LTD systems (PRF = 10 Hz) located at a slant-range of 5 km from the target (laser spot perpendicular to the target). The systems were aimed at the target by qualified FAC operators and activated for periods of 30 seconds, in the same atmospheric conditions (V = 22 km, T = 32°C and RH = 45%).

The pointing accuracy data (i.e., displacement of the energetic and geometric centres of the laser spots on the target with respect to the target centre) were obtained using the procedures described below for the three cases of slightly distorted, highly distorted and broken laser spots.

Moderately/Highly Distorted Spots: For laser spots preserving a shape almost circular and an energy profile approximately *Gaussian* (like the original laser signal at the system aperture), the geometric centre was computed as the centre of the smallest circle inscribing the laser spot. The spot energy centroid (maximum of the laser energy) was determined by using a dedicated interpolation function available with the IMAGE-PRO PLUS software (see Figure 8-27).

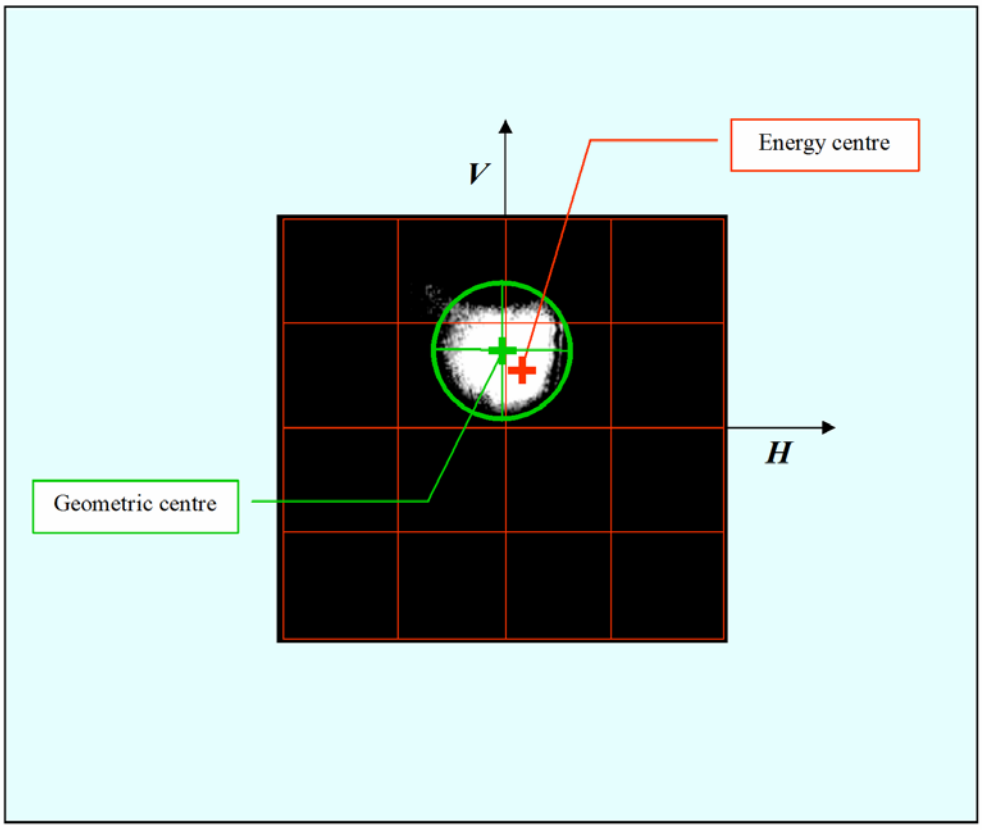

Figure 8-27: Pointing Accuracy Measurements on a Slightly Distorted Laser Spot.

An example of computations performed on a highly distorted laser spot is shown in Figure 8-28.

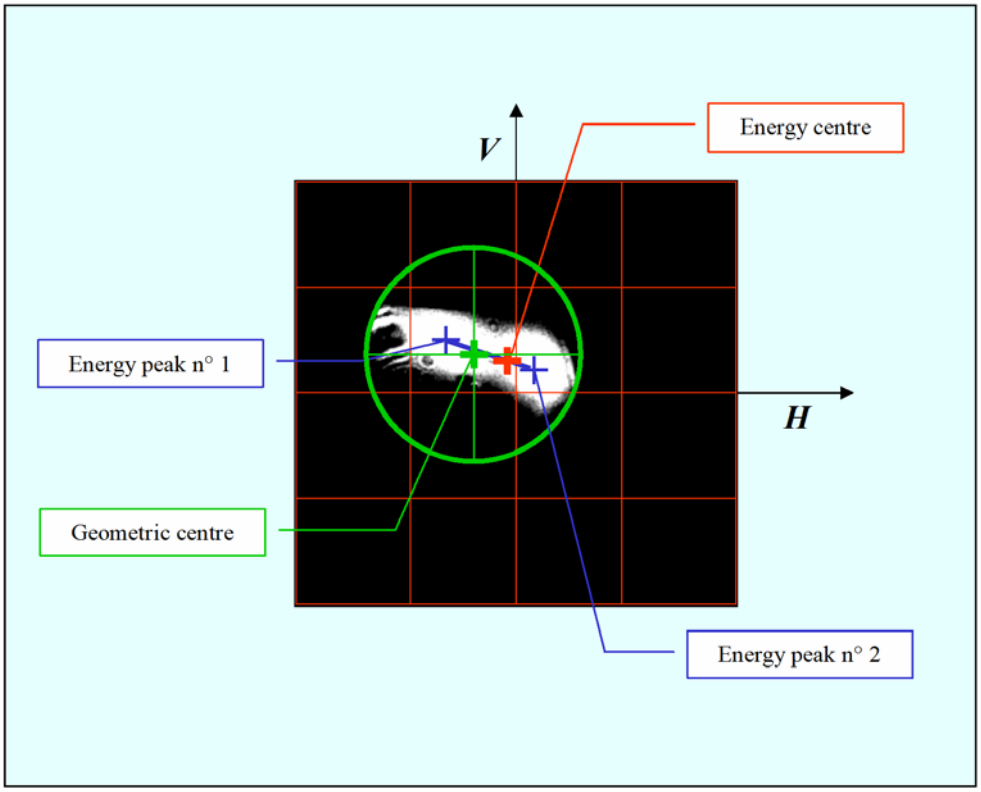

Figure 8-28: Pointing Accuracy Measurements on a Highly Distorted Laser Spot.

Broken Spots: For broken spots (with significantly high energy densities in the broken parts), the energy centre was also computed with the same IMAGE-PRO PLUS interpolation function. In this case, however, the geometric centre of the spot was computed with a dedicated algorithm, using as many circles as the broken portions (with dimensions inscribing the portions) and performing a weighted average in which the weighting factors were the ratios of the single circle radiuses to the sum of all radiuses. Low energy spot portions (with energy content minor than 1%) were not considered in the computation algorithm. A scheme relative to the algorithm used for determining the broken spot geometric centre is illustrated in Figure 8-29. An example of computations performed on a broken spot (3 parts) is shown in Figure 8-30.

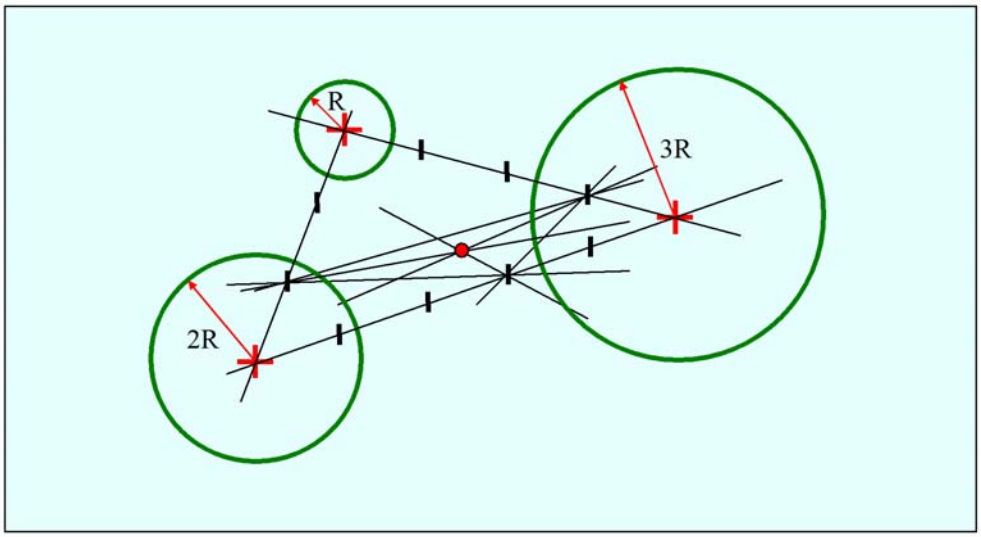

Figure 8-29: Determination of the Spot Geometric Centre (Laser Spot Broken in 3 Parts).

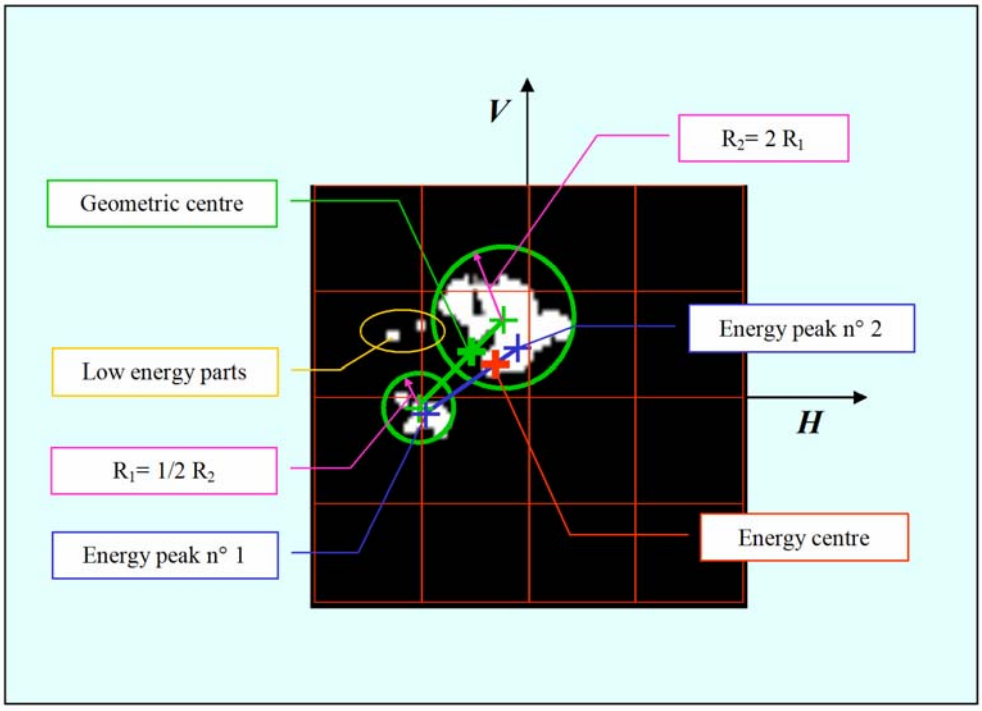

Figure 8-30: Example of Pointing Accuracy Measurements on a Broken Laser Spot.

In all cases, the position of the geometric and energetic centres was referenced to the target bi-dimensional Cartesian frame (i.e., horizontal/vertical scales and origin at the target centre). Since the operator aimed the LRF/LTD exactly at the centre of the target, the geometric and energetic pointing errors were determined (for each available spot frame) as the RSS of the horizontal and vertical error components. During these measurements, the relevant atmospheric parameters were recorded (visibility, temperature, relative humidity, wind intensity/direction, etc.).

Since the collected laser spot images were not simultaneous and the acquisition events were not synchronised, the positions of the geometric and energetic centres were computed at least 3 times for each

second (i.e., a minimum of 90 times for each system in a 30 seconds laser illumination session), and the average displacement errors of the geometric and energetic centres (i.e., average pointing errors) were calculated for each second. The results of the measurements are shown in the Figure 8-31, Figure 8-32 and Figure 8-33.

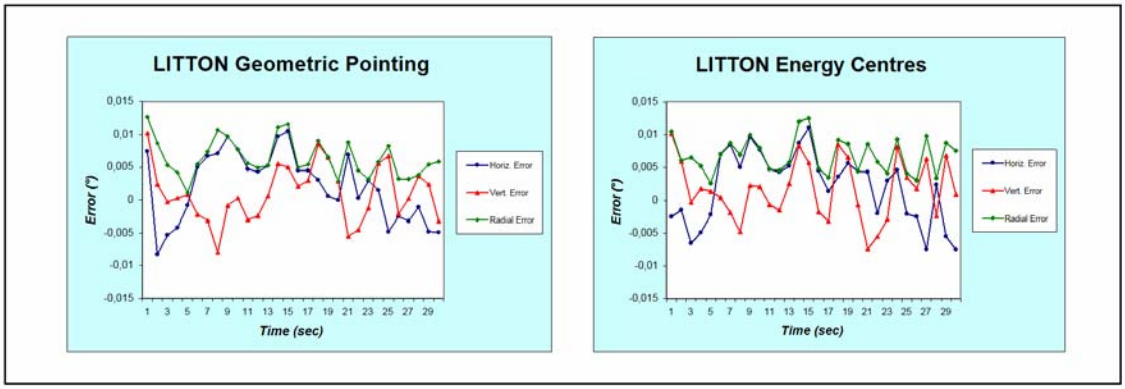

Figure 8-31: LITTON GLTD Pointing Accuracy Measurements.

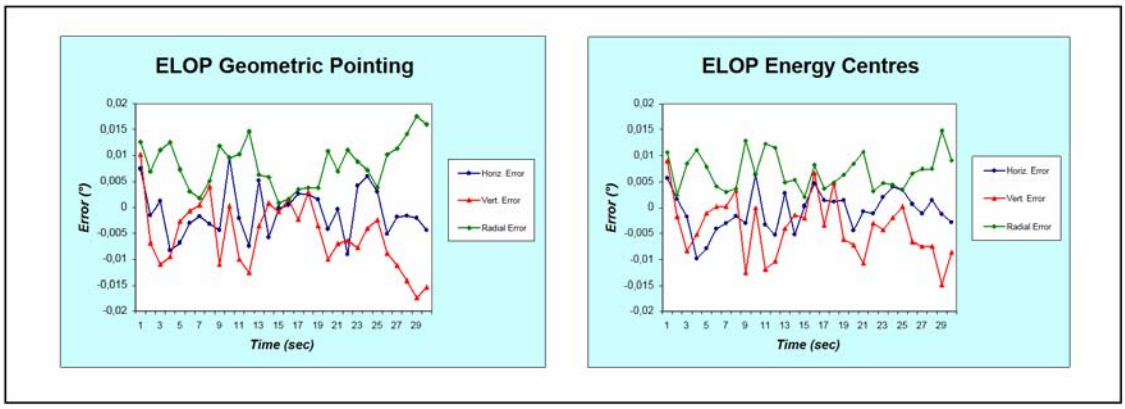

Figure 8-32: ELOP PLD Pointing Accuracy Measurements.

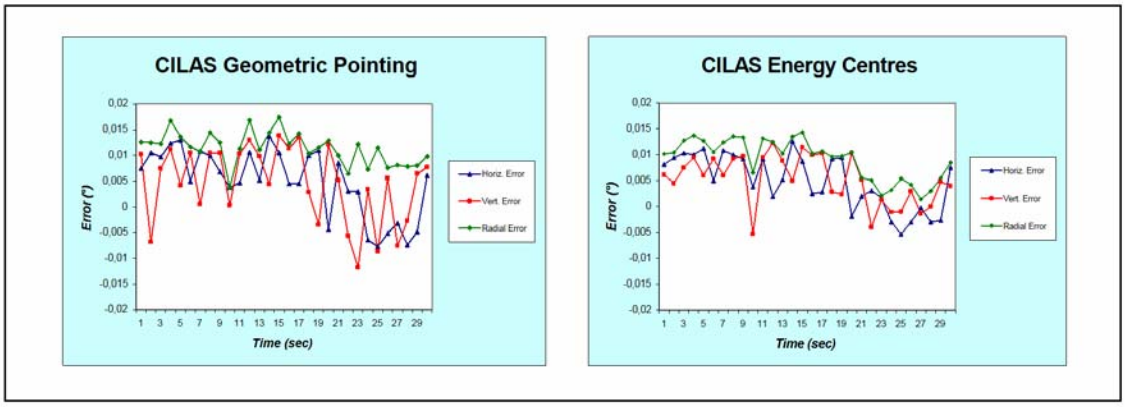

Figure 8-33: CILAS G3 Pointing Accuracy Measurements.

Figure 8-34, Figure 8-35 and Figure 8-36 show the graphs relative to the differences between geometric and energetic pointing data. Table 8-21 summarises the results of the pointing errors measurements of the three systems in terms of Geometric Pointing Accuracy (GPA) and Energy Pointing Accuracy (EPA). It is evident that the three systems had similar pointing accuracies, and that the ELOP and LITTON systems performances were slightly better than that of the CILAS system.

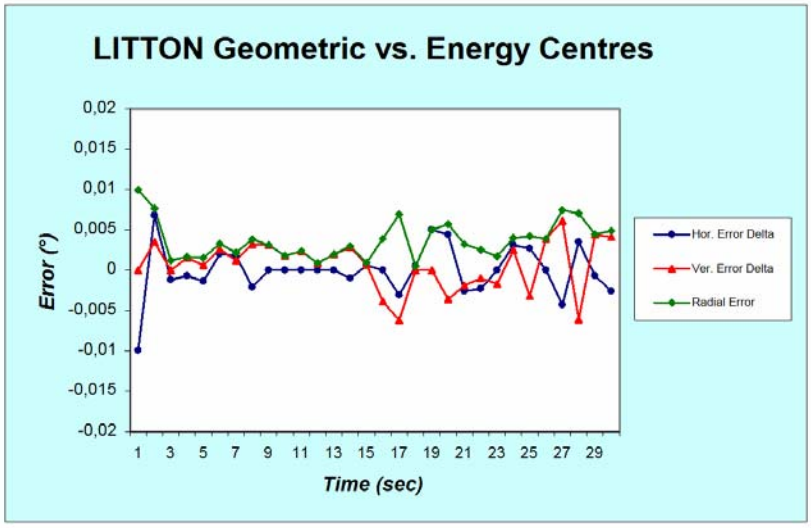

Figure 8-34: LITTON GLTD Differences in Geometric and Energy Pointing.

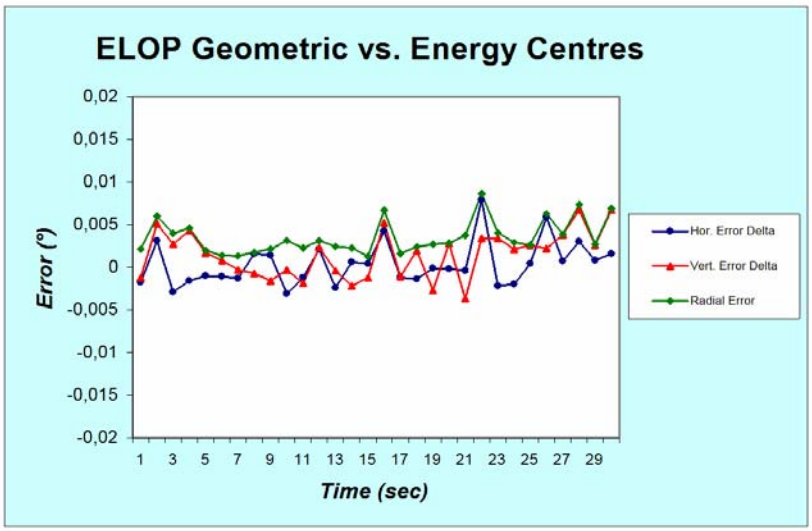

Figure 8-35: ELOP PLD Differences in Geometric and Energy Pointing.

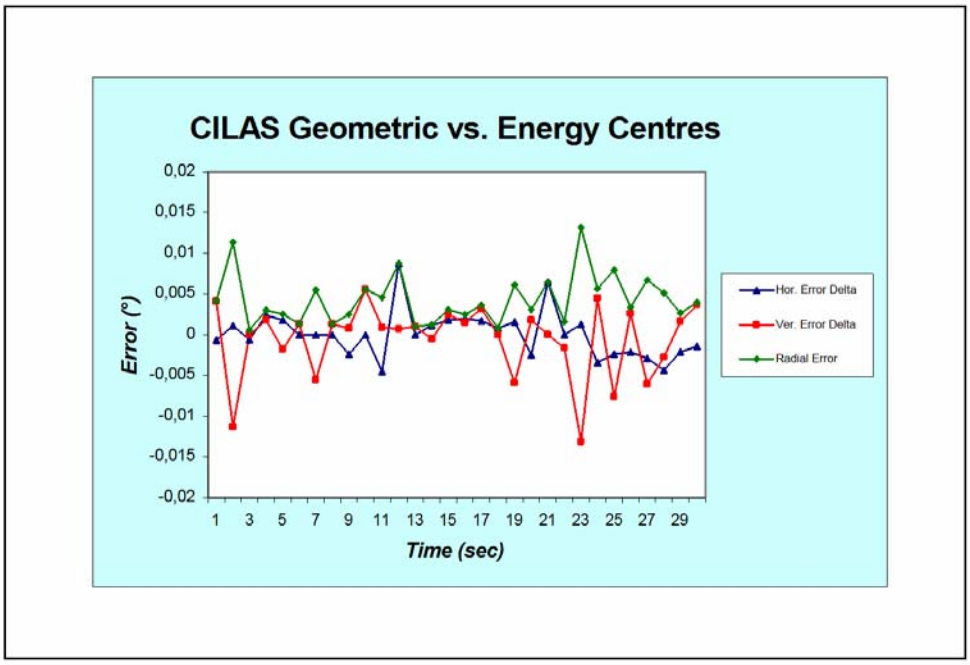

Figure 8-36: CILAS G3 Differences in Geometric and Energy Pointing.

Table 8-21: Pointing Accuracy Measurements Results

System	GPA (°)			EPA (°)			Diff- GPA-EGA (°)		
	min	max	avg	Min	max	avg	min	max	avg
LITTON	0.0011	0.0126	0.0064	0.0026	0.0125	0.0069	0.0005	0.0099	0.0037
ELOP	0.0008	0.0175	0.0083	0.0030	0.0148	0.0070	0.0013	0.0086	0.0035
CILAS	0.0038	0.0174	0.0114	0.0014	0.0143	0.0091	0.0006	0.0132	0.0052

8.2.7 Laser Spot Spreading and Distortion Measurements

Performing EMT tests at λ = 1064 nm (ELOP-PLD system), with system to target SR between 1500 m and 5.5 km, it was observed that the laser spot images collected by the Phoenix NIR-camera were characterised by a progressive increase of the spot diameters, exceeding the values predicted by theory, with increasing SR. This fact was probably due to the greater influence of both linear and non-linear propagation phenomena with longer propagation paths. In order to investigate, by monitoring the variations of the relevant meteorological parameters along the transmission paths, the effects induced by these phenomena, laser spots shapes and dimensions predicted by theory, assuming a *Gaussian* energy distribution and considering 95% of the total energy, were compared with the effective spot characteristics measured on the target. Using large data samples (i.e., 150 to 200 laser spots for each session), collected with various SR and in various weather conditions, it was possible to obtain useful data about laser spot spreading and distortion characteristics at λ = 1064 nm. The analytical methods used for spreading/ distortion measurements with moderately and highly distorted laser spots are described below.

Using the *1/e* divergence ($\Phi_{1/e}$) of the laser beam, the laser spot divergence at 95% of total energy was computed by:

$$\Phi_{95\%} = \frac{\Phi_{1/e}}{\sqrt{\frac{ln(1-0.632)}{ln(1-0.95)}}} \tag{8.56}$$

For the ELOP-PLD, since $\Phi_{1/e}$ = 0.130 mrad, we obtained $\Phi_{95\%}$ = 0.225 mrad. The expected 95%-energy laser spot radius (R) at a given distance (d) was obtained by:

$$R = d \cdot tan\, \Phi_{95\%} + a \tag{8.57}$$

where a is the output beam diameter. For instance, for the ELOP-PLD system located at SR = 5000 m, we obtained R = 1.215 m. In order to define the laser spot distortion characteristics, the following spot measurable elements were considered (see Figure 8-37):

- Radius of the smallest circle inscribing the entire spot (R_1);
- Radius of the smallest circle, centred in the spot geometric centre C, contained by the spot image (R_2); and
- Distance between energetic and geometric centres (d_{ge}).

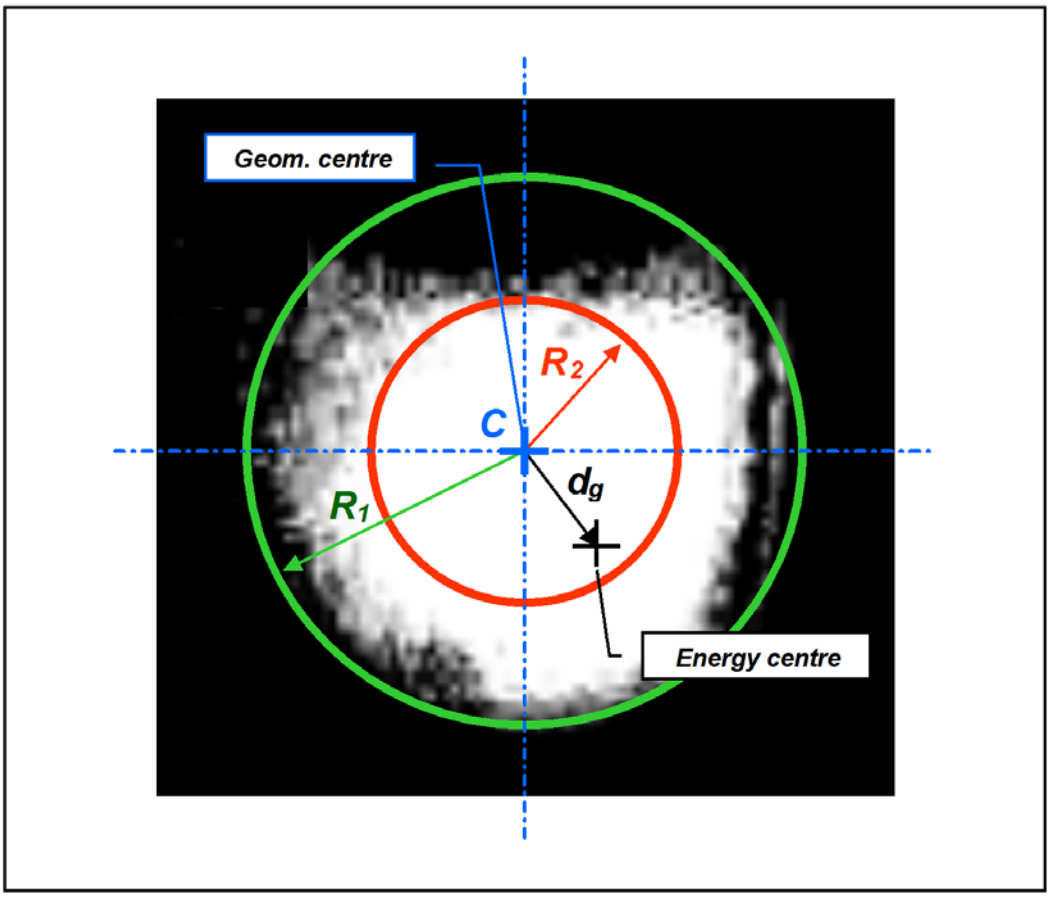

Figure 8-37: Measurable Elements Used for Distorted Spot Analysis.

These spot elements were combined to conveniently describe the spot quality in terms of spreading and distortion. Particularly, the following Spot Distortion Parameters (SDP's) were defined:

$$Q_S = \frac{R}{R_1} \tag{8.58}$$

$$Q_{De} = 1 - \frac{d_{ge}}{R_1} \tag{8.59}$$

$$Q_{Dg} = \frac{R_2}{R_1} \tag{8.60}$$

The parameter Q_S describes the spot spreading, Q_{De} is relative to the energy profile distortion and Q_{Dg} is relative to the geometric distortion of the laser spot. Conveniently, the SDP parameters were so that they equated to 1 in the ideal *Gaussian* case and tend to 0 in the worst case.

The results of the spot spreading measurements (average $2R_1$ values) are shown in Figure 8-38, together with the calculated 1/e and 95%-energy spot diameters. Although in certain cases the measured spot diameter (average of 150 – 200 measurements) was less that the calculated 95%-energy spot diameter, the average data showed that the spot spreading was much more significant at greater slant-ranges. Furthermore, it was observed that also the SDP parameters increased significantly their values at increasing slat-ranges. The average SPD values and their variations during measurements performed with the ELOP-PLD (λ = 1064 nm) at SR = 1500 m, 3.5 km and 5.5 km are listed in Table 8-22.

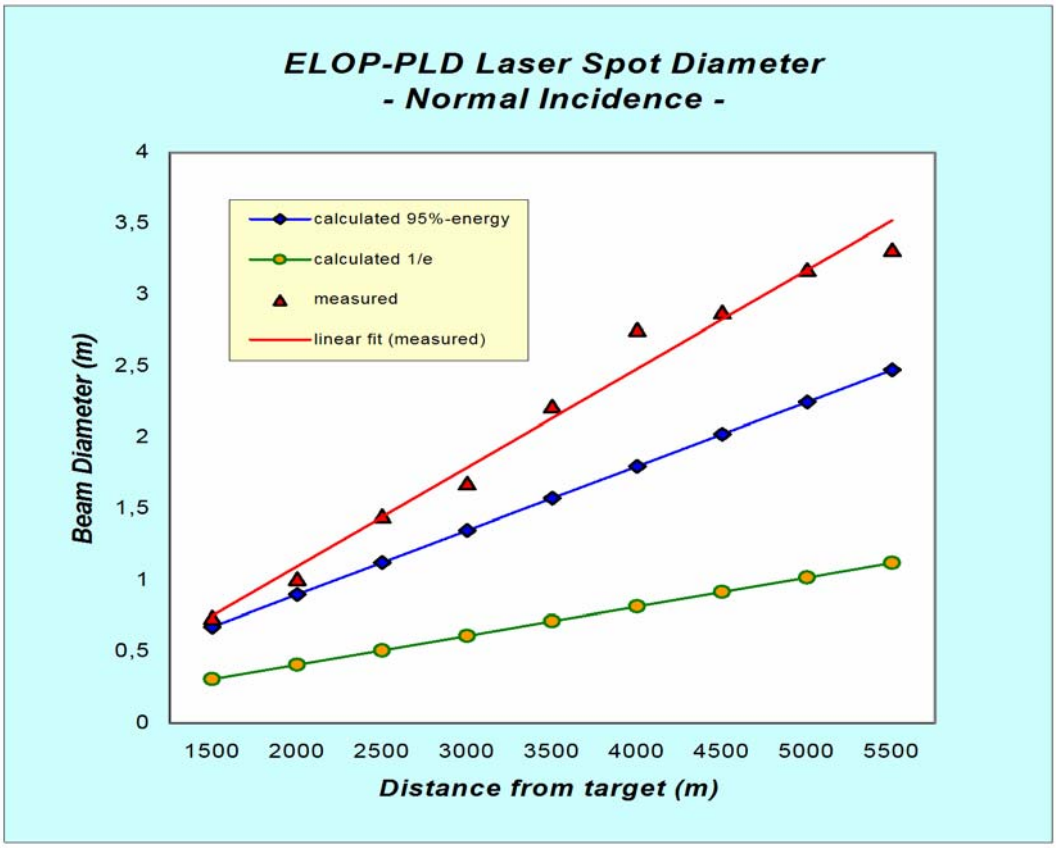

Figure 8-38: ELOP-PLD Calculated/Measured Spot Diameters for Various Slant-Ranges.

Table 8-22: SPD Parameters Relative to the ELOP-PLD Spot Distortion Measurements

SPD	1500 m		3.5 km		5.5 km	
	mean	σ	mean	σ	mean	σ
Q_S	0.8455	0.1350	0.8381	0.1799	0.6860	0.2830
Q_{de}	0.8329	0.0913	0.7184	0.1575	0.6119	0.1837
Q_{dg}	0.7275	0.1289	0.6930	0.1340	0.6607	0.1723

With increasing slant-range all SPD parameters were characterised by a progressive reduction of their mean values and greater dispersions. Therefore, although the exact nature of the correlation existing between the various SPD parameters was not identified with the data available, an additional parameter was defined in order to characterise the overall laser spot quality:

$$Q = \frac{R + R_1 + R_2 - d_{ge}}{3R_1} \tag{8.61}$$

Obviously, as all the SPD parameters vary between 0 and 1, also the Q parameter varies between 0 and 1 (ideal *Gaussian* case). The average values of the parameter Q calculated with the available ELOP-PLD data (λ = 1064 nm) were the following:

- Q = 0.8020 for SR = 1500 m;
- Q = 0.7498 for SR = 3500 m; and
- Q = 0.6529 for SR = 5500 m.

8.2.8 LOAS Ground Testing

Ground trials of the LOAS system were performed in order to verify the system detection performance in various weather conditions, and to test the validity of the mathematical models used for performance calculations. This was particularly important for preparing the LOAS flight test activity. It was in fact necessary to define a criteria for determining the system detection range performances in the worst environmental conditions, and with the worst obstacle scenarios (i.e., small wires with low reflectivity), even without performing real tests in these conditions (i.e., using experimental data collected in fear weather and with average obstacles). Mathematical modelling and ground testing of the LOAS detection performance were therefore required in order to give proper weights to the parameters playing a role in realistic operational scenarios, and to determine the target LOAS detection performances to be demonstrated in flight. Figure 8-39 illustrates this process.

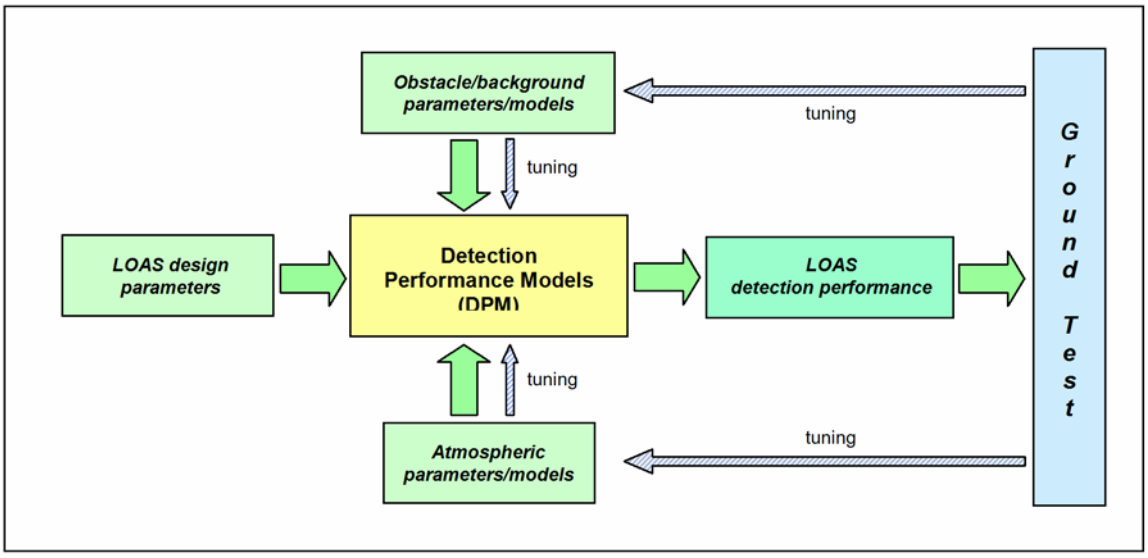

Figure 8-39: LOAS Detection Performance Modelling and Ground Testing.

As the ground test activities permitted to validate the models developed, it was then possible to identify reference sets of obstacle, background and atmospheric parameters giving the absolute minimum performance of the LOAS system. This is illustrated in Figure 8-40. Obviously, the successive flight test activities were performed only in a small portion of the LOAS/helicopter operational envelopes, but the results obtained could be extended to the entire envelopes by using the validated mathematical models.

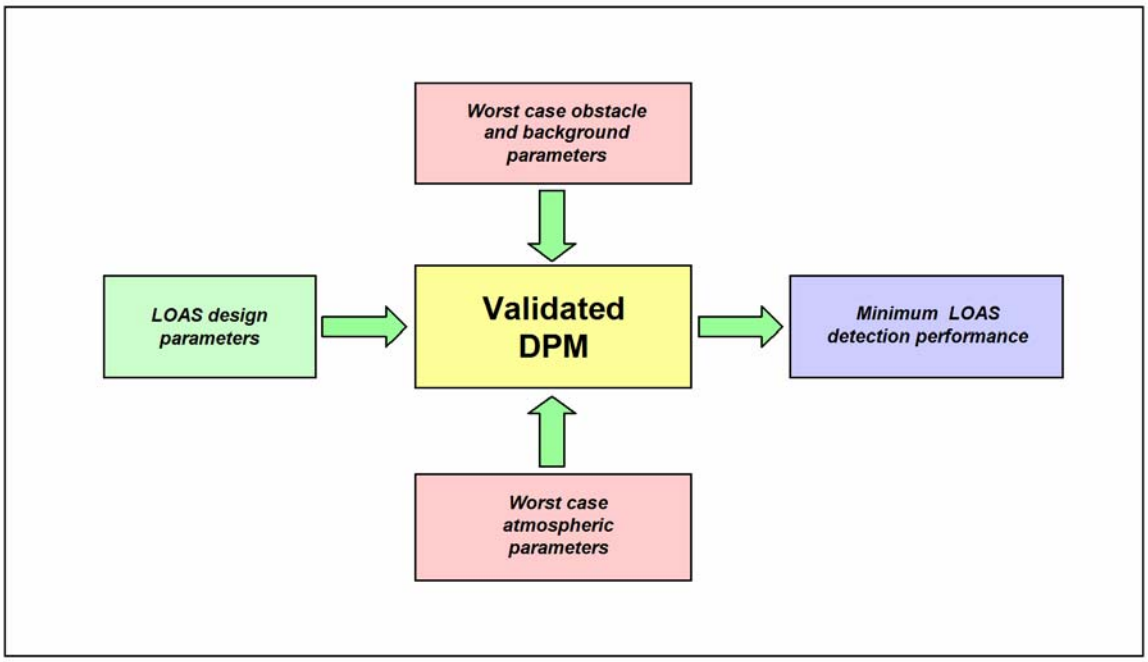

Figure 8-40: Minimum LOAS Detection Performance Calculation.

For initial design calculations, the wire obstacle detection capability of the LOAS was modelled by the following simplified Signal to Noise Ratio (SNR) equation:

$$SNR = \frac{4E_p A_r L_T L_r e^{-2\gamma R} d_W \rho}{\pi P_D R^2 (\alpha R + D) NEP} \tag{8.62}$$

where:

E_P = output laser pulse energy;
A_r = receiver aperture;
L_T = transmission losses (including beam shaping);
L_r = reception losses (including optical filter);
γ = atmospheric extinction coefficient (calculated with corrected ESLM model);
d_W = wire diameter;
ρ = wire reflectivity;
P_D = pulse duration;
R = obstacle range;
α = beam divergence (l /e^2);
D = initial beam diameter; and
NEP = noise equivalent power.

In order to estimate the SNR from experimental LOAS detector current measurements (i_{SIG}), obtained with certain obstacle ranges (R) and incidence angles (θ), SNR was expressed as follows:

$$SNR = 20 log\left(\frac{i_{SIG}(R,\theta)}{i_{NOISE}}\right) \tag{8.63}$$

The noise current terms in eq. (8.63) was modelled as:

$$i_{NOISE} = \sqrt{i_{TH}^{\ 2} + i_{BK}^{\ 2} + i_{DK}^{\ 2} + i_{RA}^{\ 2}} \tag{8.64}$$

where:

i_{TH} = thermal noise current;
i_{BK} = background noise current;
i_{DK} = dark noise current; and
i_{RA} = receiver amplifier noise.

According to the LOAS design characteristics, we had:

$$i_{BK} = \sqrt{2qP_S P_h M_A (2 + kM_A)B} \tag{8.65}$$

$$i_{TH} = \sqrt{4K_B \frac{T_k Bk}{R_L}} \tag{8.66}$$

$$i_{DK} = 0.5 \cdot 10^{-12} \tag{8.67}$$

$$i_{RA} = 1.5 \cdot 10^{-12} \tag{8.68}$$

where:

P_S = received solar power;
P_h = amplifier gain;
M_A = avalanche multiplier;
k = noise factor of the avalanche photodiode;
B = electronic bandwidth;

K_B = Boltzmann constant (1.39×10^{-23} J/°K);
T_K = absolute temperature (°K); and
R_L = amplifier load resistance.

The following characteristics were defined for a 'wire type' obstacle according to LOAS operational requirements:

- *Diameter:* 5 mm ≤ D_W ≤ 70 mm;
- *Shape:* twisted or round;
- *Reflection:* Purely diffuse (Lambertian); and
- *Reflectivity:* ≥ 20% (θ = 0).

The reference environmental parameters were set as follows:

- *Visibility:* V ≥ 800 m;
- *Humidity:* RH ≤ 100%;
- *Temperature:* T ≤ 50°C;
- *Rain:* Light/Medium/Heavy; and
- *Background:* P_B = 50 W/m^2 sr µm.

For calculation purposes, the i_{SIG} (R, θ) term in eq. (8.63), was modelled as:

$$i_{SIG} = \sqrt{\frac{P_T d_W \rho D_a^{\,3} \eta e^{-2\gamma R}}{4R^3 \lambda} \cdot \frac{P_h}{K_a} \cdot \frac{1}{R_L}} \tag{8.69}$$

where:

P_T = transmitted power;
P_h = amplifier gain;
D_a = aperture diameter; and
K_a = aperture illumination constant = $sen(\theta)^{5.4}$.

Results of range performance calculations performed with various visibilities and with all other parameters set to the worst case, are shown in Figure 8-41.

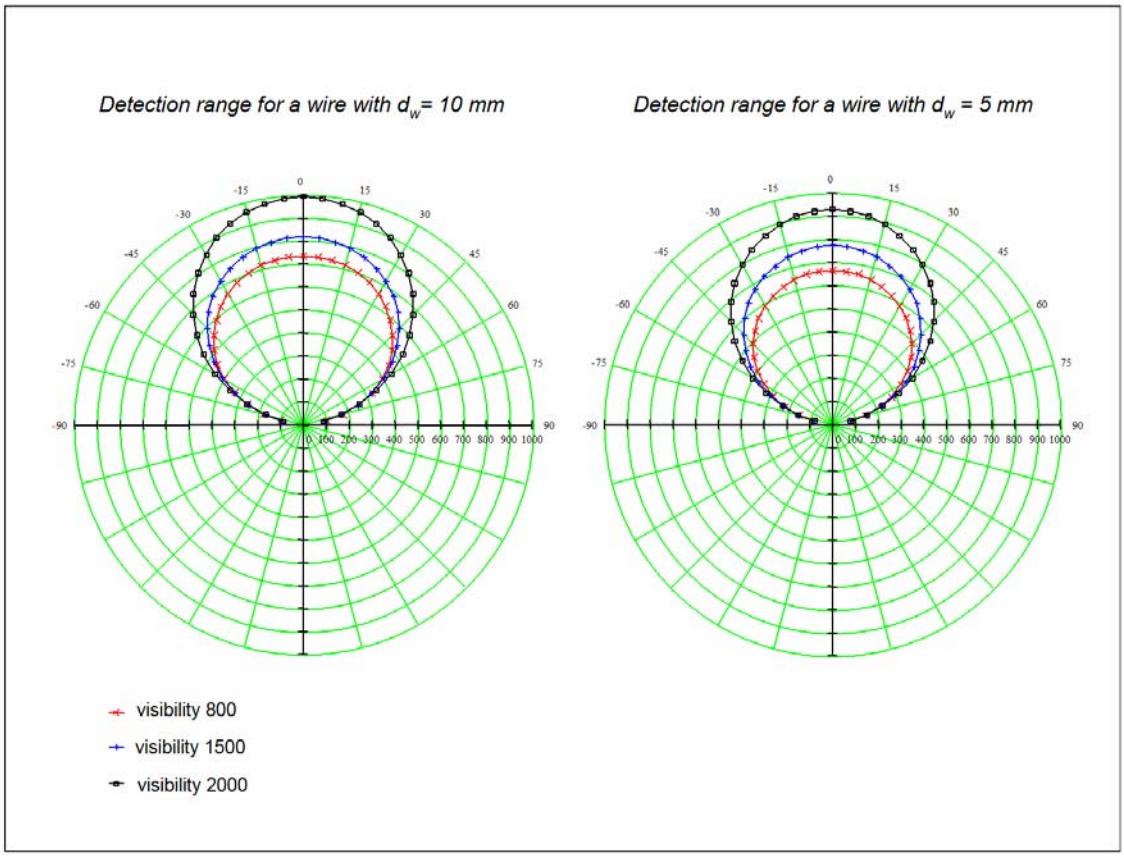

Figure 8-41: LOAS Detection Range Performance with Wires.

The false alarm probability was modelled by:

$$P_{fa} = \frac{1}{B \cdot T_{fa} \cdot \eta} \tag{8.70}$$

where:

B = receiver bandwidth;
T_{fa} = mean time between false alarms; and
η = maximum useful range/maximum non ambiguous range.

The mean time between false alarms corresponds to elementary electrical false alarms at the receiver level. The probability to have several false alarms on a straight line pattern is much lower. Statistically, these phenomena are described by the False Alarm Rate (FAR) and Detection Probability (P_d). If the noise and signal distributions are known, the SNR can be estimated and the corresponding DP and FAR can be determined. According to the Rice calculation [1], the average FAR for the LOAS system is given by:

$$\overline{FAR} = \frac{1}{2\tau\sqrt{3}} exp\left(-\frac{I_t^2}{2I_n^2}\right) \tag{8.71}$$

where:

τ = Electrical pulse length;
l_t = Threshold current; and
l_n = Average noise current.

The LOAS P_d is determined using pure *Gaussian* statistics [1], [2]:

$$P_d = \frac{1}{\sqrt{\pi}} \int_{\frac{I_t - I_n}{\sqrt{2} I_n}}^{\infty} exp\left(-\frac{i_n^2}{2I_n^2}\right) d\left(\frac{i_n}{\sqrt{2} I_n}\right) \tag{8.72}$$

where:

I_n = average signal current; and
i_n = instantaneous noise current.

The false alarm probability (P_{fa}) is given by:

$$P_{fa} = \tau \cdot \overline{FAR} \tag{8.73}$$

and the cumulative detection probability (P_D) is given by:

$$P_D = 1 - \sum_{i=0}^{m} C_M^i P_d^i \left(1 - P_d\right)^{M-i} \tag{8.74}$$

where:

M = number of possible detections; and
m = minimum number of detections required.

To validate the LOAS performance models, ground tests were performed using a wire of known section and reflectivity (D_W = 2.5 cm and ρ = 40%), and with various weather conditions (i.e., clear weather with $10 \leq V \leq 15$ km, and light/medium/heavy rain). The scenario in which ground tests were performed is shown in Figure 8-42.

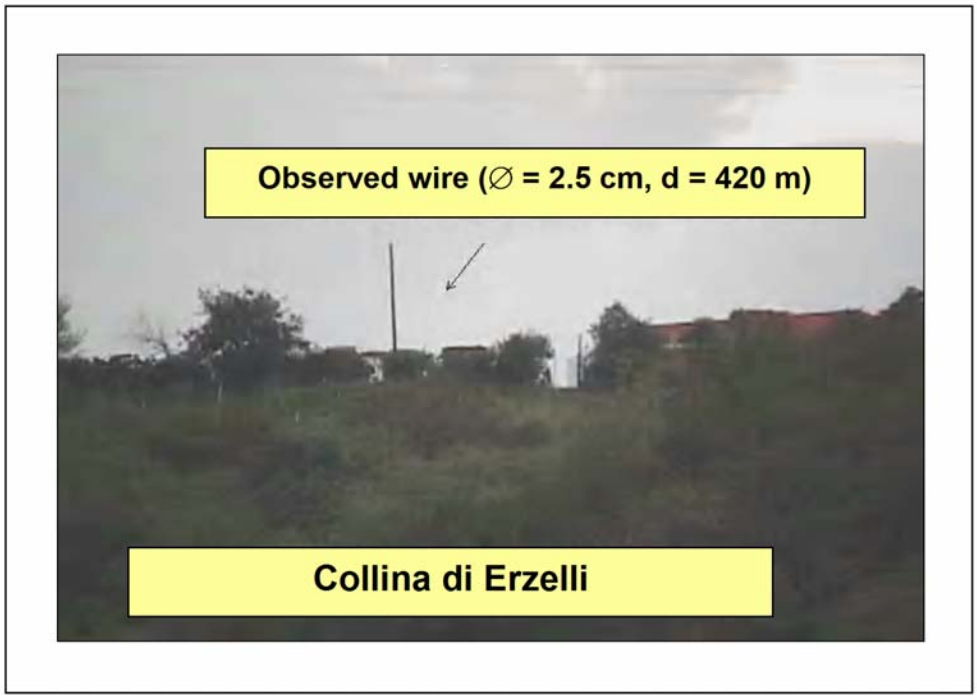

Figure 8-42: LOAS Ground Tests Scenario.

The collected data sets showed that the returned signal power fluctuates independently from pulse to pulse according to a *Gaussian* distribution. The sets of data collected in clear and rainy weather conditions are shown in Figure 8-43.

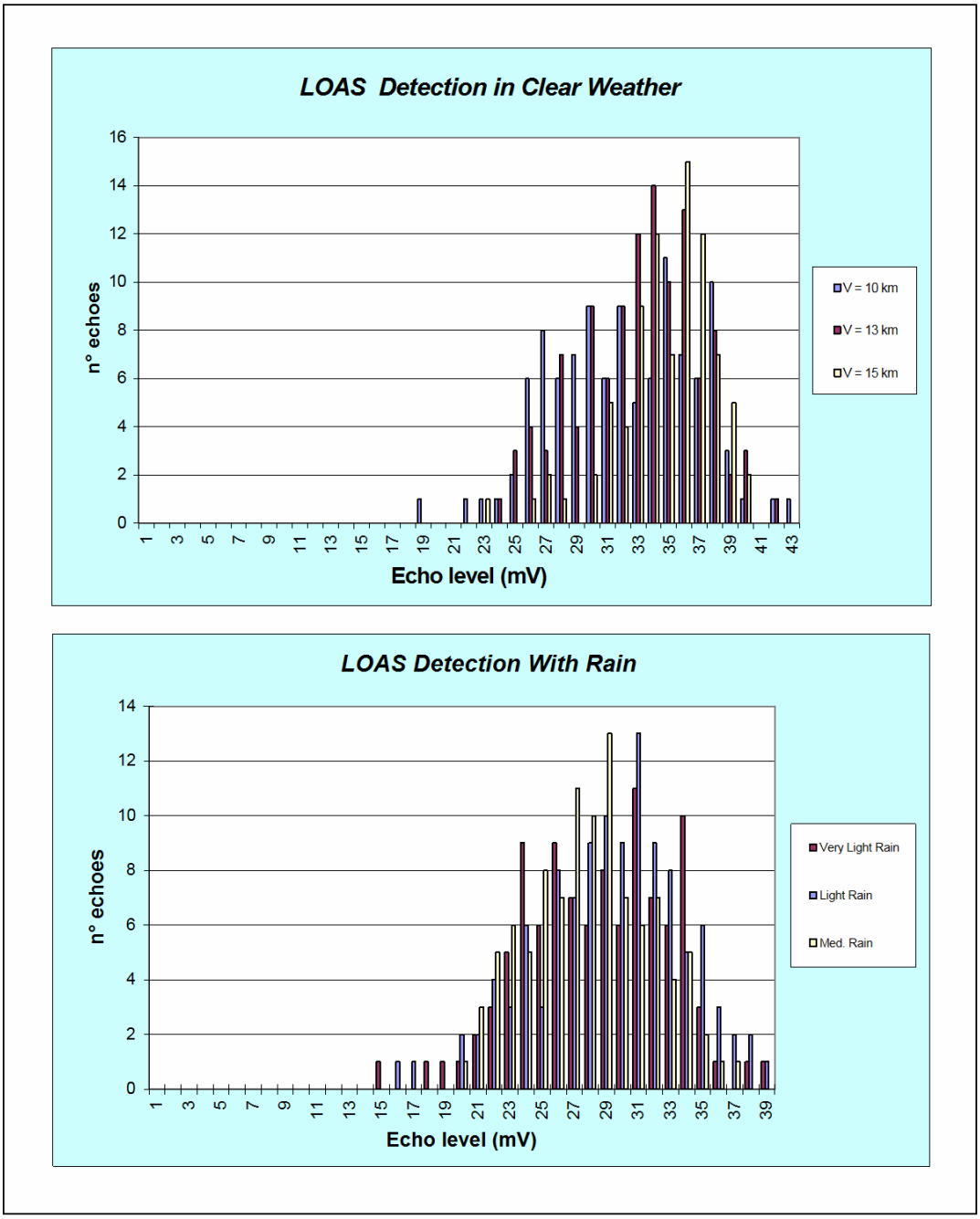

Figure 8-43: LOAS Detection Characteristics.

A comparison between the SNR predicted (SNR_P) using eq. (8.62) with γ calculated using the ESLM model (0.19 $km^{-1} \leq \gamma \leq$ 0.22 km^{-1} for clear weather and 1.23 $km^{-1} \leq \gamma \leq$ 2.94 km^{-1} for rainy conditions), assuming a background power of 10 Watt/m^2/sr/µm and ρ = 0.5, and estimated from experimental data (SNR_E) using eq. (8.63) to (8.69), is shown in Table 8-23.

Table 8-23: Comparison between LOAS Predicted and Measured SNRs

	Clear Weather			*Rain*		
	V=10 km	*V=12.5 km*	*V=15 km*	*Light*	*Medium*	*Heavy*
SNR_P	4.90×10^4	4.95×10^4	5.02×10^4	3.14×10^4	1.83×10^4	1.45×10^4
SNR_E	3.35×10^4	3.80×10^4	4.27×10^4	2.87×10^4	2.47×10^4	2.13×10^4

8.3 REFERENCES

[1] Skolnik, M.I., “Introduction to Radar Systems”. McGraw-Hill (New York). 1980.

[2] Jelalian, A.V., “Laser Radar Systems”. Artech House (Boston-London). 1992.